

GRB 160410A: the first Chemical Study of the Interstellar Medium of a Short GRB [★]

J. F. Agüí Fernández^{1†}, C. C. Thöne¹, D. A. Kann¹, A. de Ugarte Postigo^{1,2}, J. Selsing^{3,4}, P. Schady⁵, R. M. Yates⁶, J. Greiner⁷, S. R. Oates⁸, D. B. Malesani^{9,10}, D. Xu¹¹, A. Klotz¹², S. Campana¹³, A. Rossi¹⁴, D. A. Perley¹⁵, M. Blažek¹, P. D’Avanzo¹³, A. Giunta¹⁶, D. Hartmann¹⁷, K. E. Heintz^{4,18}, P. Jakobsson¹⁸, C. C. Kirkpatrick IV^{19,20}, C. Kouveliotou^{21,22}, A. Melandri¹³, G. Pugliese²³, R. Salvaterra²⁴, R. L. C. Starling²⁵, N. R. Tanvir²⁵, S. D. Vergani^{26,27} and K. Wiersema²⁸

¹Instituto de Astrofísica de Andalucía, Glorieta de la Astronomía s/n, 18008 Granada, Spain.

²Artemis, Université Côte d’Azur, Observatoire de la Côte d’Azur CNRS, F-06304, Nice, France.

³DARK, Niels Bohr Institute, University of Copenhagen, Jagtvej 128, 2200 Copenhagen, Denmark.

⁴Cosmic Dawn Center (DAWN), Niels Bohr Institute, University of Copenhagen, Jagtvej 128, 2100 Copenhagen Ø, Denmark.

⁵Department of Physics, University of Bath, Claverton Down, Bath, BA2 7AY, UK.

⁶Department of Physics, University of Surrey, Stag Hill, Guildford, GU2 7XH, UK.

⁷Max-Planck Institut für Extraterrestrische Physik, Giessenbachstr 1, 85748 Garching, Germany.

⁸School of Physics and Astronomy & Institute for Gravitational Wave Astronomy, University of Birmingham, B15 2TT, UK.

⁹DTU Space, National Space Institute, Technical University of Denmark, DK-2800 Kongens Lyngby, Denmark.

¹⁰Department of Astrophysics/IMAPP, Radboud University Nijmegen, P.O. Box 9010, 6500 GL Nijmegen, The Netherlands.

¹¹CAS Key Laboratory of Space Astronomy and Technology, National Astronomical Observatories, Chinese Academy of Sciences, Beijing 100101, China.

¹²IRAP, Université de Toulouse, CNRS, CNES, UPS, (Toulouse), France.

¹³Brera Astronomical Observatory, via Bianchi 46, I-23807, Merate (LC), Italy.

¹⁴INAF - Osservatorio di Astrofisica e Scienza dello Spazio, via Piero Gobetti 93/3, 40129 Bologna, Italy.

¹⁵Astrophysics Research Institute, Liverpool John Moores University, IC2, Liverpool Science Park, 146 Brownlow Hill, Liverpool L3 5RF, UK.

¹⁶Space Science Data Center (SSDC) - Agenzia Spaziale Italiana (ASI), Via del Politecnico, I-00133 Roma, Italy.

¹⁷Clemson University, Department of Physics and Astronomy, Clemson, SC 29634-0978, USA.

¹⁸Centre for Astrophysics and Cosmology, Science Institute, University of Iceland, Dunhagi 5, 107, Reykjavík, Iceland.

¹⁹Department of Physics, University of Helsinki, PO Box 64, FI-00014 Helsinki, Finland.

²⁰Helsinki Institute of Physics, Gustaf Hällströmin katu 2, University of Helsinki, PO Box 64, FI-00014, Helsinki, Finland.

²¹Department of Physics, The George Washington University, 725 21st Street NW, Washington, DC 20052, USA.

²²Astronomy, Physics, and Statistics Institute of Sciences (APSIS), The George Washington University, Washington, DC 20052, USA.

²³Astronomical Institute Anton Pannekoek, University of Amsterdam, PO Box 94249, NL-1090 GE Amsterdam, The Netherlands.

²⁴INAF-Istituto di Astrofisica Spaziale e Fisica cosmica, via Alfonso Corti 12, 20133 Milano, Italy.

²⁵School of Physics and Astronomy, University of Leicester, University Road, Leicester, LE1 7RH, UK.

²⁶GEPI, Observatoire de Paris, PSL University, CNRS, 5 Place Jules Janssen, 92190 Meudon, France.

²⁷Institut d’Astrophysique de Paris, UMR 7095, CNRS-SU, 98 bis boulevard Arago, 75014 Paris, France.

²⁸Physics Department, Lancaster University, Lancaster, LA1 4YB, UK

Accepted XXX. Received YYY; in original form ZZZ

arXiv:2109.13838v2 [astro-ph.HE] 5 Jan 2023

ABSTRACT

Short gamma-ray bursts (SGRBs) are produced by the coalescence of compact binary systems which are remnants of massive stars. GRB 160410A is classified as a short-duration GRB with extended emission and is currently the farthest SGRB with a redshift determined from an afterglow spectrum and also one of the brightest SGRBs to date. The fast reaction to the *Neil Gehrels Swift Observatory* alert allowed us to obtain a spectrum of the afterglow using the X-shooter spectrograph at the Very Large Telescope (VLT). The spectrum shows several absorption features at a redshift of $z = 1.7177$, in addition, we detect two intervening systems at $z = 1.581$ and $z = 1.444$. The spectrum shows Ly α in absorption with a column density of $\log(N(\text{HI})/\text{cm}^2) = 21.2 \pm 0.2$ which, together with Fe II, C II, Si II, Al II and O I, allow us to perform the first study of chemical abundances in a SGRB host galaxy. We determine a metallicity of $[X/H] = -2.3 \pm 0.2$ for Fe II and -2.5 ± 0.2 for Si II and no dust depletion. We also find no evidence for extinction in the afterglow Spectral Energy Distribution (SED) modeling. The environment has a low degree of ionisation and the C IV and Si IV lines are completely absent. We do not detect an underlying host galaxy down to deep limits. Additionally, we compare GRB 160410A to GRB 201221D, another high- z short GRB that shows absorption lines at $z = 1.045$ and an underlying massive host galaxy.

Key words: neutron star mergers – gamma-ray burst: individual: GRB 160410A – gamma-ray burst: individual: GRB 201221D – galaxies: ISM

1 INTRODUCTION

For a brief moment, gamma-ray bursts (GRBs) are capable of outshining any other source in the Universe. Their γ -ray flashes can last from significantly less than a second to hundreds or even thousands of seconds (Kouveliotou et al. 1993). According to their duration and spectral characteristics, GRBs can be divided into two classes, long/soft GRBs (LGRBs) and short/hard GRBs (SGRBs). LGRBs are associated with the collapse of very massive stars and their prompt γ -ray emission in most cases lasts for more than 2 s. They have been shown to be linked to broad-lined Type Ic core-collapse supernovae (e.g. Galama et al. 1998; Hjorth et al. 2003; Woosley & Bloom 2006; Hjorth & Bloom 2012; Cano et al. 2017).

SGRBs, in contrast, are associated with the merger of a binary system of compact objects, usually two neutron stars (NSs, Berger 2014; Abbott et al. 2017b). They show a harder γ -ray spectrum than LGRBs and have a T_{90}^1 of less than 2 s (Kouveliotou et al. 1993), although some events show extended emission (EE), albeit with a softer spectrum, and recently, an event, GRB 211211A, which was almost indistinguishable from a long GRB, has been associated with a compact object merger (Rastinejad et al. 2022; Gompertz et al. 2022; Yang et al. 2022; Troja et al. 2022). SGRB afterglows are typically less luminous than those of LGRBs (Kann et al. 2011) which makes them much more difficult to detect at higher redshifts. A recent study by Dichiaro et al. (2021) suggests that at high redshifts, there is a bias towards SGRBs with extended emission as they are typically brighter than regular short GRBs.

In a SGRB, during coalescence of the binary system, a relativistic jet forms producing the prompt emission and later the afterglow emission by interaction with the circumburst environment, the same way the afterglow is produced for LGRBs. SGRBs also show a so-called *kilonova* emission (KN), powered by the radioactive decay of heavy elements produced via the r -process in a neutron-rich environment (Metzger et al. 2010). The KN emission is normally much

fainter than the afterglow and hence is only detected a few days after the GRB when the afterglow has faded (e.g. Metzger 2019).

Until recently, GRBs have only been detected by high-energy instruments on-board satellites such as the *Neil Gehrels Swift Observatory* (*Swift* hereafter)/Burst Alert Telescope (BAT, Gehrels et al. 2004; Barthelmy et al. 2005), *Fermi*/Gamma-Ray Burst Monitor (GBM, Meegan et al. 2009), or *Konus-Wind* (Aptekar et al. 1995). In 2017 a gravitational wave (GW) was detected by LIGO/Virgo together with a corresponding electromagnetic counterpart at various wavelengths and the SGRB 170817A detected by *Fermi*/GBM and the SPI-ACS (SPECTrometer on INTEGRAL - Anti-Coincidence Shield) on *INTEGRAL* just ~ 1.7 s after the GW detection, firmly linking NS mergers to SGRBs (Goldstein et al. 2017; Savchenko et al. 2017; Abbott et al. 2017b,a; Tanvir et al. 2017). However, to date this has been the only event where an electromagnetic counterpart has been detected in association with a GW signal from a NS-NS merger (e.g. Antier et al. 2020). Optical surveys of the sky such as the Zwicky Transient Facility (ZTF) are expected to significantly increase the KN detection rate, even in the absence of a γ -ray or GW signal (Bellm et al. 2019; Graham et al. 2019; Andreoni et al. 2021).

The presence of KN emission has been claimed for a small number of SGRBs, however, the first conclusive detection was obtained for GRB 130603B (Tanvir et al. 2013; Berger et al. 2013). This SGRB was also the first showing absorption lines in the afterglow spectrum (de Ugarte Postigo et al. 2014a). Since then, only a few SGRBs had a redshift spectroscopically determined via the afterglow. This makes the study of the redshift distribution and properties of the interstellar medium (ISM) challenging for the class of SGRBs and often only an indirect redshift via association with a likely host galaxy is available (e.g. Berger 2010).

Short bursts are associated with host galaxies featuring a wide distribution of stellar population ages and galaxy types. SGRBs do not seem to have a preferred location in their host galaxies. Some have even been detected at large distances from their putative hosts (e.g. Leibler & Berger 2010; Berger 2010; Fong & Berger 2013). The offset distribution can be explained by the time needed for the compact objects to form from their massive star binary progenitors and the subsequent delay time for the system to merge due to GW energy loss (Beniamini & Piran 2019; Belczynski et al. 2006; Paterson et al. 2020).

Several studies suggest compact object mergers (NS-NS, or Neu-

* Based on observations made with telescopes at the European Southern Observatory at La Silla/Paranal, Chile under programme 097.A-0036(A).

† E-mail: feli@iaa.es

¹ T_{90} is defined as the time span during which from 5% to 95% of the total counts emitted by a GRB are detected.

tron Star - Black Hole, NS-BH) as a major source for r -process element enhancement (Watson et al. 2019; Roederer et al. 2016) in dwarf galaxies (Beniamini et al. 2015) as well as in ultra-faint dwarf (UFD) galaxies (Beniamini et al. 2016a). This is the case for Reticulum II, a UFD containing very metal-poor stars with a higher abundance of r -process elements than expected from chemical evolution driven by typical core-collapse supernovae (CC-SNe). It has been suggested that a single NS-NS merger could generate the r -process element abundances observed in these galaxies, however, rare CC-SNe cannot be ruled out (Ji et al. 2016a; Beniamini et al. 2016b).

In contrast, long GRBs are commonly found in bright, metal-poor regions within their host galaxies (e.g. Fruchter et al. 2006; Jakobsson et al. 2006; Thöne et al. 2008; Lyman et al. 2017) and typically with large neutral hydrogen column densities. Most LGRB hosts have $\log(N(\text{HI})/\text{cm}^2) > 20.3$ (e.g. Tanvir et al. 2019), which is the definition for a Damped Ly α (DLA) system. LGRBs have proven to be ideal beacons in the study of neutral and ionised gas evolution in absorption in the ISM, the Circumgalactic Medium (CGM) and the Intergalactic Medium (IGM) (e.g. Wolfe et al. 2005; Starling et al. 2013; Selsing et al. 2019; Bolmer et al. 2019; Gatkin et al. 2019).

In this paper we present a study of the optical counterpart of GRB 160410A and its afterglow spectrum. GRB 160410A is the first SGRB for which the spectral observations span a large enough spectral range, together with the SGRB redshift, to cover the Ly α absorption line and has sufficient quality to make a chemical study of the gas in its host galaxy. We also include GRB 201221D in our analysis, a SGRB with absorption lines in the spectrum, which had a lower redshift of $z = 1.045$ and a less broad spectral coverage (see Sect. 2.6). The paper is structured as follows: In Sect. 2 we present the observations of the afterglow and host galaxy of both GRBs, Sect. 3 presents the results on the analysis of the spectrum of the burst afterglow and its light curve as well as observations of the field to detect the host galaxy. For GRB 201221D we also present the analysis and properties of its associated host galaxy. In Sect. 4 we put the results in context of similar studies for long GRBs and in Sect. 5 we present our final conclusions.

Throughout this study, we adopt a cosmological model with $H_0 = 67.3 \text{ km s}^{-1} \text{ Mpc}^{-1}$, $\Omega_M = 0.315$, $\Omega_\Lambda = 0.685$ (Planck Collaboration et al. 2014).

2 OBSERVATIONS

2.1 High-energy detection of GRB 160410A

Swift/BAT triggered on a source at RA = $10^{\text{h}} 02^{\text{m}} 43^{\text{s}}$, Dec. = $+03^\circ 26' 37''$ with an uncertainty of $3'$ on the 10^{th} of April, 2016 at 05:09:48 UT (Gibson et al. 2016). The event localisation was refined by the UVOT instrument on-board *Swift* that took a finding chart with the *white* filter with a total exposure time of 150 s only 91 s after the BAT trigger, locating the burst to RA = $10^{\text{h}} 02^{\text{m}} 44.37^{\text{s}}$, Dec. = $+03^\circ 28' 42.7''$ with an uncertainty of $0''.49$ (Marshall & Gibson 2016). In the refined analysis of Sakamoto et al. (2016) the burst shows a duration of $T_{90} = 8.2 \pm 1.6$ s in the 15 – 350 keV band and a spectral lag of 8 ± 14 ms between the 50 – 100 keV and 15 – 25 keV bands and -3 ± 7 ms between the 100 – 350 keV and 25 – 50 keV bands, which is consistent with zero, as expected for SGRBs (Norris & Bonnell 2006). The BAT light-curve analysis of Sakamoto et al. (2016) shows signs of faint extended emission, $\sim 0.038 \text{ counts det}^{-1} \text{ s}^{-1}$ at T+10 s.

The *Swift* X-Ray Telescope (XRT, Burrows et al. 2005) observed

the GRB at five epochs starting from 83 s after the GRB. Data were initially acquired in Windowed Timing (WT) mode due to the brightness of the source, and later in Photon Counting (PC) mode. The XRT light curve shows an initial steep decay with a power law decay index of 2.0 ± 0.1 , and possibly two small flares superimposed. The light curve continued with a flattening, starting from ~ 750 s followed by another decay. However, the XRT data collected in PC mode are too sparse to provide a deeper analysis of the lightcurve.

Observations from *Konus-Wind*, sensitive to higher energies in the 20 keV–10 MeV range, show a peak energy of $E_{\text{peak, observed}} = 1416_{-356}^{+528}$ keV, a $T_{90} = 2$ s, and an isotropic energy release of $E_{\text{iso, rest}} = 4.0 \times 10^{52}$ erg (Frederiks et al. 2016). However, Frederiks et al. (2016) used a different cosmology than the one adopted in this work so we re-calculated it (see Sect. 4.1 and Appendix A). Given the energy released as observed by *Konus-Wind*, the initial pulse complex (Frederiks et al. 2016), the extended softer emission (Dichiara et al. 2021), and the negligible spectral lag (Sakamoto et al. 2016), this burst has been classified as a short GRB with extended emission (see Sect. 4.1 and Appendix A for further discussion on this issue).

2.2 X-shooter observations of GRB 160410A

The X-shooter spectrograph (Vernet et al. 2011) was automatically triggered after the *Swift* alert using the Rapid-Response Mode (RRM). Observations of the afterglow of GRB 160410A started at 05:18:08.00 UT, 8.4 minutes after the *Swift* trigger. The acquisition image showed the afterglow at $r' = 20.249 \pm 0.037$ mag (AB photometric system). The initial results of the analysis of the spectrum were reported by Selsing et al. (2016)². The observations consisted of a total of 3 exposures of 600 s each in a dithering pattern ABB taken just before the twilight and before the telescope limit at 20° elevation was reached. The seeing was $\sim 0''.9$ and transparency conditions were clear. Due to the high airmass (~ 2.4) at which the observation was performed, the spectral trace changes its position on the slit as a function of wavelength, which we modelled in the spectral extraction. The spectra were reduced using the ESO/X-shooter pipeline v.2.6.8 (Modigliani et al. 2010) and Reflex (Freudling et al. 2013). The final spectrum has a spectral resolution in the UVB arm of 54 km s^{-1} and of 28 km s^{-1} in the VIS arm. No features were detected in the NIR arm. An initial sky-subtraction was performed on the unrectified image. The spectral response function was generated using observations of a spectrophotometric standard-star (Vernet et al. 2010; Hamuy et al. 1994) with an optimal extraction, as was also done for the science spectrum. We show the complete normalised spectrum in Fig. 1. The signal-to-noise (SNR) per resolution element varies between ~ 5 – 15 in the UVB arm and between ~ 7 – 10 for the VIS arm for the continuum in the regions where we detect absorption lines. In the NIR we find an average SNR of ~ 1.2 .

2.3 Photometric Observations of GRB 160410A

For our analysis of the GRB we also obtained imaging of the optical and near-IR afterglow of GRB 160410A. In addition to the observations listed below, we used the acquisition image of the X-shooter observations (see Sect. 2.2) as well as literature data from Skynet PROMPT (Trotter et al. 2016) and a late detection by the 2.4 m

² We note that this spectrum was also presented as part of the X-shooter sample by Selsing et al. (2019).

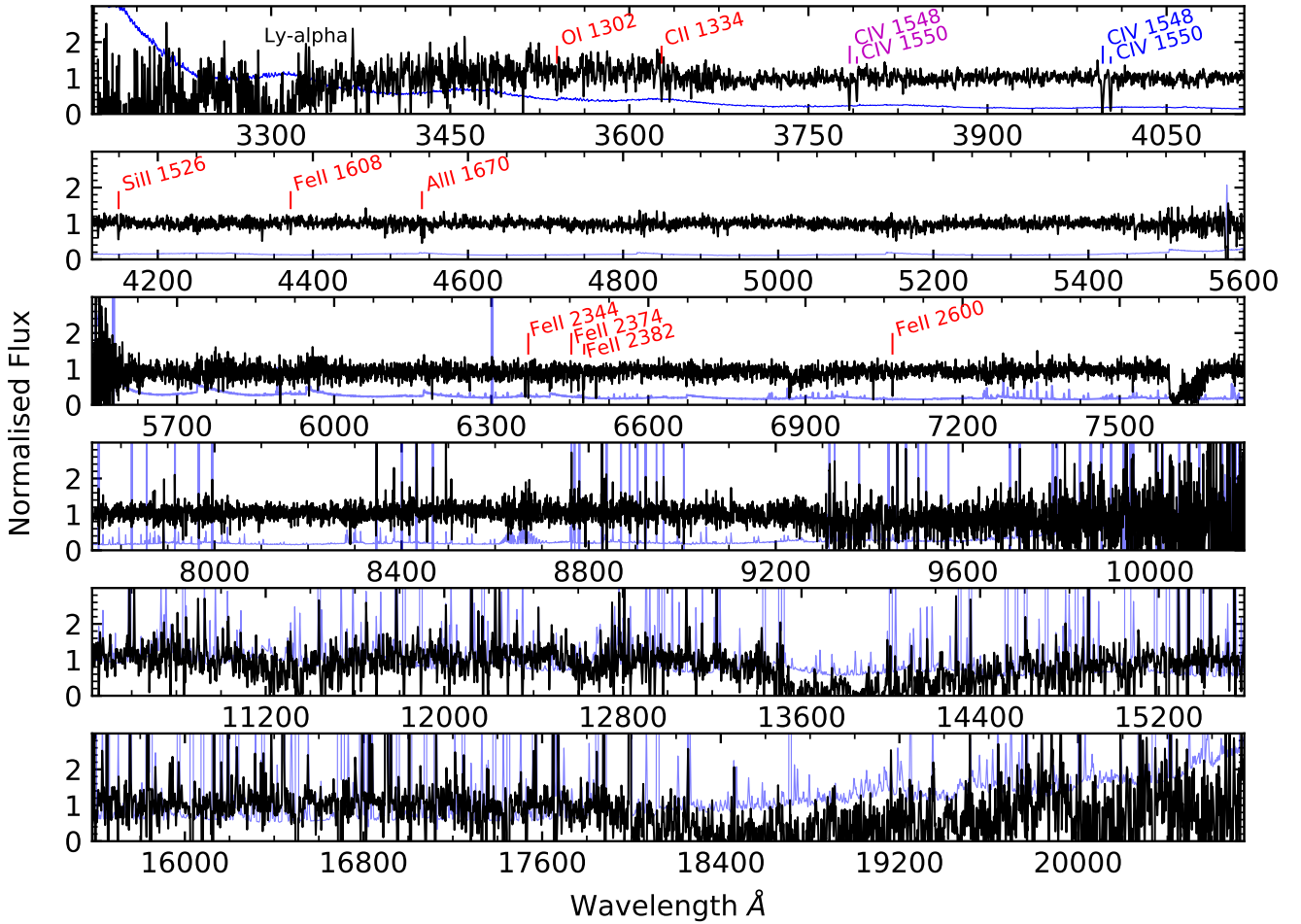


Figure 1. X-shooter spectrum (black) of the optical afterglow of GRB 160410A smoothed using a Gaussian kernel with 1σ for the first four panels and 2σ for the last two panels showing the NIR spectrum. The error spectrum is plotted in blue for the unbinned spectrum. Vertical lines denote the absorption lines: Red corresponds to absorption lines at the GRB redshift, blue is the intervening system at $z = 1.581$, and magenta the intervening system detected at $z = 1.444$. The error spectrum in the blue end is higher than the actual spectrum due to the absence of binning for the error spectrum.

GMG telescope (Wang et al. 2016). For our analysis, we do not use the afterglow limits reported by Muraki et al. (2016); Juvan et al. (2016); Cobb (2016); Rastinejad et al. (2021). Finally, we obtained late observations of the field in the optical with the 10.4 m Gran Telescopio de Canarias (GTC) and in infrared with the *Spitzer* space observatory to search for an underlying host galaxy (see Sects. 2.4.1, 2.4.2 and Fig. 2).

2.3.1 TAROT observations

The 0.25 m Télescope à Action Rapide pour les Objets Transitoires (TAROT) La Silla telescope observed the location of GRB 160410A very rapidly, beginning 28 s after trigger (16.8 s after notice). Observations (originally published in Klotz et al. 2016) were obtained in trailing mode (Klotz et al. 2006). The afterglow is detected as a very faint trail. The photometry method was based on the division of the afterglow flux by the flux of a reference star. To verify the validity of the method we chose another known star as a check. The magnitudes of the two stars ($r' = 13.517$ mag, $r' = 16.720$ mag, respectively) were taken from the Sloan Digital Sky Survey (SDSS) Data Release

12 (Alam et al. 2015). To evaluate the flux density uncertainties we computed the standard deviation of the background. The check star allowed us to validate the photometric method since the SDSS magnitude lies fully within the computed limits for each measurement. The TAROT best mean magnitude is 0.08 mag fainter than the SDSS value, however, the TAROT image is unfiltered, explaining this small colour effect.

The afterglow evolution shows a decay with a possible superposed flaring behaviour (see Sect. 3.4). We note that the columns on which the afterglow trail was located from 55 – 60 s are less sensitive than the surrounding ones and we can only claim an upper limit here. Furthermore, the afterglow magnitude fell below the detection limit by the end of the trailed observation.

2.3.2 UVOT observations

The *Swift*/UltraViolet Optical Telescope (UVOT, Roming et al. 2005) began observing the field of GRB 160410A 91 s after the *Swift*/BAT trigger. Observations were taken in both event and image modes. The afterglow is detected in all UVOT filters except for *uvw2* and

*uv*m2, as these lie blueward of $\text{Ly}\alpha$ at the redshift of GRB 160410A. Before extracting count rates from the event lists, the astrometry was refined following the methodology of Oates et al. (2009). The source counts were extracted initially using a source region of $5''$ radius. When the count rate dropped to below 0.5 counts/s, we used a source region of $3''$ radius. In order to be consistent with the UVOT calibration, these count rates were then corrected to $5''$ using the curve of growth contained in the calibration files. Background counts were extracted using three circular regions of radius $10''$ located in source-free regions. The count rates were obtained from the event and image lists using the *Swift* tools *uvotevt1c* and *uvotsource*, respectively. They were converted to magnitudes using the UVOT photometric zero points (Poole et al. 2008; Breeveld et al. 2011). To improve the signal-to-noise ratio, the count rates in each filter were binned using $\Delta t/t = 0.2$, leading to longer but deeper exposures at later times. The early event-mode *white* and *u* finding charts were bright enough to be split into multiple exposures.

2.3.3 GROND observations

We obtained multi-band photometric observations with the Gamma-Ray burst Optical and Near-infrared Detector (GROND) (Greiner et al. 2008; Greiner 2019) mounted on the 2.2 m MPG telescope at ESO La Silla observatory (originally published in Yates et al. 2016) in the $g'r'i'z'JHK$ bands. GROND observations began about half an hour after the GRB, at very high airmass (2.7). Only a single 4M4TD³ observation Block (OB) could be obtained before the telescope hit a pointing limit. The effective integration time was somewhat reduced by the low quality of one of the dithering positions. However, the afterglow is still detected in $g'r'i'z'$. The following night, observations started at lower airmass but under adverse conditions. A total of 28 8M4TD OBs were obtained, but only OBs 1 – 21 were usable. The afterglow had faded considerably, and was only detected in $g'r'i'$.

Afterglow magnitudes in the optical were calibrated against standard stars in the same field from the SDSS catalogue (Alam et al. 2015). Near-infrared magnitudes (all upper limits) were measured against comparison stars in the field taken from the 2MASS catalogue (Skrutskie et al. 2006). Reduction and analysis were performed within a custom pipeline calling upon IRAF tasks (Tody 1993), following the methods of Krühler et al. (2008); Yoldaş et al. (2008).

2.3.4 NOT observations

Observations were taken in the r' band with the Alhambra Faint Object Spectrograph and Camera (AlFOSC) at the 2.5 m Nordic Optical Telescope (NOT) at the Roque de la Muchachos Observatory on La Palma, Canary Islands, Spain (originally published by Malesani & Kirkpatrick 2016; Malesani et al. 2016, see Fig. 2). The afterglow was directly calibrated against four SDSS stars in the field. In the second epoch, forced aperture photometry on the afterglow position yields a tentative 3σ detection, which, however, is in agreement with the decay extrapolated from earlier times. We therefore include it as a detection.

³ Denoting the integration time in the NIR is 4 min in total, and there are four optical images at four different dithering positions, therefore a 4M(inute)4T(elescope)D(ithers).

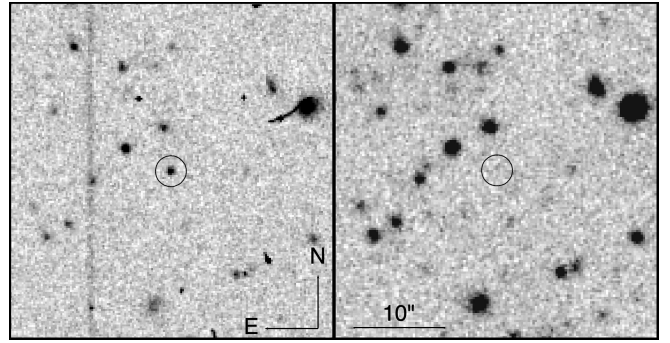


Figure 2. Optical observations of the field of GRB 160410A. *Left:* r' -band image obtained by NOT 0.7 days after the burst where the afterglow is clearly detected. *Right:* Deep late observation at 44.7 days in the same band by the 10.4 m GTC, where no source is detected down to a limit of $r' > 27.17$ mag (AB, corrected for Galactic extinction).

2.4 Host observations of GRB 160410A

We performed deep photometric observations with a ground-based facility in search of an underlying galaxy hosting GRB 160410A. We also observed with the IRAC instrument on-board the *Spitzer* satellite.

2.4.1 GTC observations

We searched for a possible underlying host galaxy at the GRB position at late times in the r' band using OSIRIS at GTC. Data were taken on the night of the 24th of May 2016, comprising a total of ten images with an exposure time of 180 s each⁴. The observations were obtained at an airmass of ~ 1.4 and calibrations were performed using four SDSS field stars. We do not detect any source at the position of the afterglow down to a 3σ limit of 27.17 mag (AB, corrected for Galactic extinction) (see Fig. 2).

2.4.2 Spitzer observations

We obtained observations of the field of GRB 160410A with the Infrared Array Camera (IRAC) on-board the *Spitzer* Space Telescope on 2017 August 22 as part of the extended *Swift/Spitzer* GRB Host Galaxy Legacy Survey (SHOALS; Perley et al. 2016a). One hour of integration (36×100 s dithered images) was obtained in IRAC channel 1 ($3.6 \mu\text{m}$). We downloaded the *Spitzer* Post-Basic Calibrated Data (PBCD) co-added images from the *Spitzer* Heritage Archive and used the methods of Perley et al. (2016b) to model and subtract nearby contaminating sources within a $20''$ box around the location of the GRB. There is no source visible consistent with the location of the optical afterglow in this image. We derive a 3σ limit on the magnitude within a $2''$ aperture centred on the GRB afterglow location of $m_{ch1} > 24.74$ mag (AB).

2.5 High-Energy detection of GRB 201221D

Swift/BAT detected the short GRB 201221D at 23:06:34 UT on 21 December 2020 (Page et al. 2020). The burst is located at RA = $11^{\text{h}} 24^{\text{m}} 14.09^{\text{s}}$, Dec. = $+42^{\circ} 08' 40.0''$ (J2000) with an uncertainty

⁴ Observations obtained under GTC programme GTC22-16A (PI: C.C. Thöne).

of $\sim 1''.1$. It had a duration of $T_{90} = 0.16 \pm 0.04$ s in the 15–350 keV band (Krimm et al. 2020) and a peak energy in observer frame of 98 ± 8 keV as seen in *Fermi*/GBM observations (Hamburg et al. 2020). GRB 201221D was observed by the *Konus-Wind* observatory showing a peak energy of $E_{\text{peak, observed}} = 148^{+86}_{-37}$ keV (Frederiks et al. 2020), which implies that it was a clear short GRB.

2.6 GTC Spectroscopic observations of GRB 201221D

We observed the GRB afterglow using GTC/OSIRIS starting 2.76 hours after the trigger. The observations consisted of an acquisition image in r' band followed by long slit spectroscopy⁵. Four exposures of 1200 s were obtained covering the 3700 Å to 7800 Å spectral range, at an airmass ranging from 1.45 to 1.83.

The data were reduced using a self-developed pipeline based on IRAF routines. Data reduction included bias and response correction, and wavelength calibrations using HgAr and Ne lamps, which were also used to do a 2D distortion correction. Cosmic rays were removed using the `lacos_spec` routine (van Dokkum 2001). The flux calibration was performed using as reference the spectrophotometric standard star G191B2B (Oke 1990). The 1D spectrum was obtained through optimal extraction (Horne 1986).

This is the first afterglow spectrum of a short GRB showing evidence for absorption lines obtained since GRB 160410A and only the third spectrum of a short GRB afterglow to have them, which is why we include it in this paper for comparison. The spectrum shows emission and absorption features while the continuum is dominated by the host galaxy (see Sect. 3.5). Unfortunately the low signal-to-noise ratio of the spectrum of GRB 201221D limits the amount of information that can be extracted from these data.

2.7 Host observations of GRB 201221D

The Large Binocular Telescope (LBT) observed the underlying host galaxy of GRB 201221D at two epochs. A first observation was obtained on the 24th of December, 2020 when we observed in the near-infrared J and K_s filters with the LBT Utility Camera in the Infrared (LUCI, Seifert et al. 2003) imager and spectrograph under good seeing with $1''.0$ on average, (first reported in Rossi & CIBO Collaboration 2021). The second observation was obtained the 10th of January, 2021 in the $g'r'i'z'$ bands with the Large Binocular Camera (LBC, Giallongo et al. 2008) under moderate seeing conditions ($1''.6$ on average).

LBT data were reduced using the data reduction pipeline developed at INAF-Osservatorio Astronomico di Roma (Fontana et al. 2014) that includes bias subtraction and flat-fielding, bad pixel and cosmic ray masking, astrometric calibration and coaddition. For LUCI, it includes also dark subtraction and sky subtraction. The astrometry was calibrated against field stars in the GAIA DR2 catalogue (Gaia Collaboration et al. 2018) and has an astrometric precision of $0''.15$.

All data were analysed by performing aperture photometry using DAOPHOT and APPHOT under PyRAF/IRAF. We have carefully selected the size of the apertures to avoid faint sources close to the host, in particular a faint source $3''.5$ NW from the host. The photometric calibration was performed in the optical against the SDSS DR12 catalogue (Alam et al. 2015) and in the NIR against 2MASS stars.

⁵ Observations obtained under GTC programme GTCMULTIPLE2G-20B (PI: de Ugarte Postigo).

3 ANALYSIS AND RESULTS

Our comprehensive analysis of the GRB 160410A afterglow comprises data from high energies to optical wavelengths. Unfortunately, no near-infrared data of sufficient quality are available. For GRB 201221D, the data coverage is significantly sparser than for GRB 160410A.

3.1 X-Ray analysis of GRB 160410A

We extracted the spectrum in WT mode, avoiding the small flares (i.e., in the 89 – 150 s time-frame) collecting ~ 700 source counts. This is to avoid possible contamination from the flare emission on the spectral parameters. We fitted the X-ray data with a power-law model, with the Galactic absorption fixed to $N_{\text{H, Gal}} = 1.8 \times 10^{20}$ cm⁻² and a free intrinsic absorption at $z = 1.72$ of the host galaxy. We adopted C-statistics and data were binned to 1 count per energy bin in the 0.3 – 10 keV energy range. The best-fit power-law photon index is $\Gamma = 1.6 \pm 0.1$ (1σ confidence level). The intrinsic absorption column density is $N_{\text{H}}(z) = 3.0^{+2.3}_{-1.9} \times 10^{21}$ cm⁻². The spectrum evolves to a softer value as the flux decreases ($\Gamma \sim 2$), but the lower number of counts prevented us to better constrain the photon index.

3.2 Spectral analysis

In the spectrum of GRB 160410A we detect several absorption features typically found in long GRB sight-lines (Christensen et al. 2011). The wavelength coverage of X-shooter allows the detection of Ly α absorption from a host galaxy DLA system at the blue end of the spectrum which, together with other metallic lines, is used to derive the metallicity of the host galaxy gas. We do not detect any fine-structure lines commonly associated with gas in the close GRB environment (Vreeswijk et al. 2007, 2011; D'Elia et al. 2009a,b). For Fe II* λ 2612 we derive a rest frame limit of $< 0.15\text{\AA}$ a value 30% lower than what has been measured for this line in a GRB composite spectrum (Christensen et al. 2011). However, the absorption lines observed are very weak so the non-detection of fine-structure lines is consistent with their relative strength in the aforementioned composite spectrum.

The lines observed are only in the UVB and VIS arms, neither emission nor absorption features are observed in the NIR arm. Selsing et al. (2016) reported a first determination of the redshift of GRB 160410A, based on the detection of Fe II and Al II absorption lines, resulting in a value of $z = 1.717$. In our analysis, we find additional features, not mentioned in the original GCN, of O I, C II and Si II at the same redshift. Contrary to the claim in Cao et al. (2016), we detect neither the C IV λ 1548, 1550 doublet in our spectrum, nor Mg II λ 2976, 2803 doublet. The non-detection of high-ionisation lines, commonly seen in other GRB sight-lines (Christensen et al. 2011), point to a low ionisation environment. The Mg II lines fall inside the telluric A-band and can therefore not be recovered in our spectrum. Emission lines would fall as well in the NIR and are not detected, which is not surprising given the high redshift, the non-detection of a host galaxy (see Sect. 3.3) and the fact that the emission lines fall in regions with strong telluric features or high noise levels.

In Tab. 1 we list the detected features and their corresponding equivalent widths (EW). Line identifications and measurements were obtained using the tools in the GRBspec database (de Ugarte Postigo et al. 2014b; Blažek et al. 2020). The different absorption lines are centred at slightly different redshifts due to different velocity components (see Sect. 3.2.1) and we obtain a non-weighted mean value

Table 1. Observed absorption-line list for the spectrum of GRB 160410A. Top: lines at the redshift of the GRB. We include the 3σ limits derived for Si IV and C IV (see Sect. 3.2.3). Middle and bottom parts: C IV absorbers detected at $z = 1.581$ and $z = 1.444$ respectively. The first column shows the absorption line ID and its rest-frame wavelength. The second column lists the corresponding centroid for the redshifted absorption line. The third column is the measured EW in the rest frame, the fourth column is the total column density we derive using the VoigtFit fitting code (Krogager 2018) for each transition.

Feature	Observed wavelength (Å)	EW (Å)	$\log(N)$ (cm^{-2})
Ly α 1215.670	3304	–	21.20 ± 0.20
O I 1302.170	3539.4000	0.32 ± 0.08	> 15.04
C II 1334.530	3626.9869	0.26 ± 0.08	> 14.77
Si II 1526.710	4149.5107	0.33 ± 0.06	14.25 ± 0.11
Al II 1670.790	4540.6191	0.29 ± 0.07	13.13 ± 0.21
Fe II 1608.450	4371.3224	0.17 ± 0.04	14.32 ± 0.09
Fe II 2344.210	6370.6764	0.35 ± 0.08	...
Fe II 2382.770	6475.4289	0.36 ± 0.06	...
Fe II 2374.460	6452.9438	0.19 ± 0.06	> 14.22
Fe II 2586.650	7029.2700	0.35 ± 0.04	...
Fe II 2600.170	7066.1812	0.30 ± 0.05	...
Si IV 1393.760	–	< 0.36	> 13.60
Si IV 1402.770	–	< 0.39	> 13.93
C IV 1548.200	–	< 0.24	> 13.76
C IV 1550.770	–	< 0.24	> 14.06
C IV 1548.200	3996.2713	0.57 ± 0.06	> 14.82
C IV 1550.770	4002.9657	0.52 ± 0.06	...
C IV 1548.200	3784.1820	0.38 ± 0.07	> 14.91
C IV 1550.770	3790.4285	0.27 ± 0.07	...

of $z = 1.7177 \pm 0.0001$, which matches the redshift of the strongest Fe II component.

3.2.1 Absorption line fitting

We fitted Voigt profiles to the observed lines at the GRB redshift to obtain column densities, including the broad Ly α absorption. The spectrum was normalised and as systemic redshift we adopted the strongest velocity component of the Fe II λ 2600 line as $v = 0 \text{ km s}^{-1}$. For the line fitting we used the VoigtFit fitting code (Krogager 2018) that allows to define and tie parameters for each component such as the b -parameter, the column density or the redshift. We find that, for most of the detected transitions, the absorption can be fitted to two components while for Al II and up to three Fe II lines we find only one component. For Fe II λ 1608, 2344, 2382 and Si II the line profile is fitted well using two components and tying them for Si II to the ones of Fe II. However, for O I and C II, the first component is fitted to a broader b -parameter. For Fe II λ 2374, 2586, 2600 and Al II, only first component is well fitted. The non-detection of the second component for this Fe II transitions might imply that we are underestimating the amount of Fe II in this lines. This could be due to the low resolution of the spectrum or the low amount of Fe II at this second component. We therefore adopt the measured column density for Fe II λ 2374, 2586, 2600 lines as limits and choose the measures for Fe II λ 1608, 2344, 2382 as values.

In Tab. 1 we present the total measured column density for each line. The O I and C II lines are likely saturated hence we consider

them as lower limits, something which could also explain the different metallicity value obtained from these two lines. The fitting results are shown in Tab. 2. We plot the lines in velocity space in the normalised spectrum in Fig. 3, centered at the main component. The absorption lines show a small offset towards higher velocities in the absorption lines detected in the VIS arm compared to the UVB arm (see Fig. 3). A similar shift in wavelength has been reported in the past between the VIS and NIR arms of X-shooter and also suggested for the UVB arm as a problem related to the wavelength calibration (see e.g. Selsing et al. 2019; Gonneau et al. 2020).

In the spectrum of GRB 160410A, the broad Ly α absorption lies at the very blue end of the X-shooter wavelength coverage, where the continuum is rather noisy (see Fig. 4). However, we were able to determine the column density using VoigtFit and masking the blue wing from -1000 km s^{-1} . We obtain a total column density of $\log(N(\text{HI})/\text{cm}^2) = 21.2 \pm 0.2$, which is consistent with Selsing et al. (2019) and puts the system in the category of DLAs. The column density is also close to the median value that is found in long GRB spectra, i.e. $\log(N(\text{HI})/\text{cm}^2) = 21.59$ (Tanvir et al. 2019).

3.2.2 Metallicity

GRB 160410A is currently the only SGRB event where we are able to study the metallicity along the sight-line in its host galaxy. The different ions of C, O, Si, Al and Fe give slightly different metallicities. The values for C and O can only be considered as lower limits since the absorption lines are likely saturated. The metallicity values derived from Si, Al and Fe are very similar and consistent within errors (see Tab. 2). All the metallicity values are very low, even compared to the uncorrected metallicities for dust-depletion for LGRB environments (see Fig. 6).

Dust depletion can affect the observed abundances when large fractions of refractory elements are locked into dust grains. We performed a dust depletion correction on our observed metallicities following the method developed by De Cia et al. (2013, 2016, 2018). In these studies, the correction was based on the [Zn/Fe] ratio but, since we did not detect Zn we used the observed Si II line to derive [Zn/Fe]_{exp} using the following relation from De Cia et al. (2018) with their corresponding fitting parameters $A_{1, \text{Si}}$ and $B_{1, \text{Si}}$ as derived in De Cia et al. (2016).

$$[\text{Zn}/\text{Fe}]_{\text{exp}} = \frac{[\text{Si}/\text{Fe}] - A_{1, \text{Si}}}{B_{1, \text{Si}} + 1}$$

We found a ratio of [Si/Fe] = -0.08 ± 0.15 and, with $A_{1, \text{Si}} = 0.26$ and $B_{1, \text{Si}} = -0.51$, we got that [Zn/Fe]_{exp} = -0.69 ± 0.32 implying no depletion. However, De Cia et al. (2018, see their Appendix A) state that $A_{1, \text{Si}}$ and $B_{1, \text{Si}}$ might not be very well constrained.

We performed the same analysis including only the component at $v = 0 \text{ km s}^{-1}$. Using values for this first component (see Tab. 2) we got [Si/Fe] = -0.18 ± 0.18 , resulting in [Zn/Fe]_{exp} = -0.90 ± 0.40 . Furthermore, we derived δ_X , a parameter that indicates how much an observed element is depleted by dust (De Cia et al. 2016), for both, the total absorption and only for the component defined at $v = 0 \text{ km s}^{-1}$. In Fig. 5 we plot the dust depletion pattern compared to the sequence expected for different amounts of depletion derived in De Cia et al. (2016). In both cases, the values that we obtain would formally result in negative depletion and hence nonphysical values. This indicates that there is no depletion in the system and, therefore, we adopt zero values for the depletion, as shown in Fig. 5.

Our analysis results in a very low value of [Fe/H] = -2.3 ± 0.2 for the metallicity along the sight-line. To put the value into the context of cosmic chemical evolution, we compared our results with

Table 2. Column densities derived fitting a Voigt profile to the different velocity components in the absorption system at the GRB redshift. We also show the corresponding derived metallicities. $v = 0 \text{ km s}^{-1}$ corresponds to the Fe II line at 2600 \AA as the line with the highest S/N. Solar metallicities are photospheric, meteoric, or the average value between the two, following [Lodders et al. \(2009\)](#)

Ions	Transitions (\AA)	Component I			Component II			[X/H]
		v (km s^{-1})	b (km s^{-1})	$\log(N)$ (cm^{-2})	v (km s^{-1})	b (km s^{-1})	$\log(N)$ (cm^{-2})	
Fe II	2374, 2586, 2600	0	15	> 14.21	–	–	–	> -2.44
Al II	1670	13.13 ± 0.21	–	–	–	-2.50 ± 0.30
Fe II	1608, 2344, 2382	0	15	14.27 ± 0.10	74	18	13.31 ± 0.10	-2.34 ± 0.22
Si II	1526	14.10 ± 0.15	74	18	13.69 ± 0.16	-2.46 ± 0.23
O I	1302	0	22	> 14.53	74	18	> 14.84	> -2.85
C II	1334	> 14.65	> 14.03	> -2.86

those shown by [De Cia et al. \(2018\)](#), which are corrected for dust depletion following the single-reference method (see Fig. 6). The metallicities in the QSO-DLA sample have been determined using the Fe II absorption and are dust-corrected ([De Cia et al. 2018](#)). We note that [De Cia et al. \(2018\)](#) relax the DLA condition to a slightly lower column density ($\log(N(\text{HI})/\text{cm}^2) \geq 20.0$, [De Cia et al. 2016, 2018](#)) than the common definition of a DLA system ($\log(N(\text{HI})/\text{cm}^2) \geq 20.3$, [Wolfe et al. 2005](#)), however, the number of QSOs outside the strict DLA definition is small. In addition, we include DLAs in long GRB hosts from the literature, not corrected for dust-depletion as QSO-DLA and GRB 160410A are and, therefore, not formally comparable. We clearly see the existence of an observational bias on redshift that results from the realistic spectral coverage when obtaining GRB spectroscopy⁶. We note a small tendency of long GRB-DLAs towards higher metallicities (see e.g. [Fynbo et al. 2008](#); [Prochaska et al. 2007](#)), which is consistent with LGRBs tracing more enriched gas than QSO-DLAs as an effect of tracing gas in star-forming regions. However, since LGRB-DLA metallicities are not dust-depletion corrected, the differences between both samples might be somewhat larger. From the QSO-DLA sample, we clearly see that GRB 160410A shows one of the lowest metallicity values for a DLA, together with a few QSO-DLAs.

3.2.3 Line strength and host ionisation

[de Ugarte Postigo et al. \(2012\)](#) established a new parameter to compare the ISM of different GRBs by determining the relative ratio between the EWs of different lines with the average EW of (long) GRBs. We apply this method to the spectrum of GRB 160410A using the EW measurements listed in Tab. 1. We see that all EWs measured for GRB 160410A are lower than these of the long GRB sample by more than 1σ . This, together with the large column density measured for the neutral hydrogen, are indicative of low metallicity, which is consistent with the values we derive in sec. 3.2.2. We obtain a value for the Line Strength Parameter of $\text{LSP} = -1.92 \pm 1.07$, implying that the features detected in GRB 160410A are only 0.7% as strong

⁶ As GRB afterglows fade within hours or days, spectroscopy is generally obtained with ground-based facilities, and the atmospheric ultraviolet cutoff implies that Ly α is only measurable at $z \gtrsim 1.5$ ([Updike et al. 2008](#)). Detection of Ly α enabling lower redshift metallicity determinations would need an UV-capable space-based spectrograph such as HST/COS or Swift/UVOT grism spectroscopy, with the latter needing an extremely bright afterglow such as in the case of GRB 191221B ([Kuin & Swift/UVOT Team 2019](#)).

(or 99.3% weaker) as the average strength of long GRB absorption lines.

Fig. 7 shows how all the spectral features that we measured are well below the lower $1\text{-}\sigma$ region for the EW of the sample. This difference is even stronger in the case of high-ionisation features. The C IV and Si IV limits that we derive are further away from the lower $1\text{-}\sigma$ EWs of the sample than the C II and Si II lines. This is indicative of a low ionisation.

The low ionisation is clearly seen in Fig. 8, where we plot the line ratios C IV/C II and Si IV/Si II of our sight-line, as compared to the sample of [de Ugarte Postigo et al. \(2012\)](#). In the case of GRB 160410A, we use the $3\text{-}\sigma$ limits to the detection of C IV and Si IV. GRB 160410A is located in the lower left area of the diagram, just outside the $1\text{-}\sigma$ region of the sample, amongst the lowest ionisation sight-lines of the sample. The moderate S/N of our spectrum prevents us from showing stronger limits to the high-ionisation lines.

3.2.4 Intervening systems

In the afterglow spectrum we detect two further systems in the line-of-sight as already mentioned by [Selsing et al. \(2019\)](#), at redshifts $z = 1.581$ and $z = 1.444$. Both show the C IV $\lambda\lambda$ 1548, 1550 doublet, but no other features were detected due to the low S/N of the spectrum. We perform a Voigt fitting to both C IV absorbers by defining a broad component at $v = 0 \text{ km s}^{-1}$ with a b -parameter of $b = 40 \text{ km s}^{-1}$ for the doublet. The fitting results are plotted in Fig. 9, resulting in a total column density of $\log(N/\text{cm}^2) > 14.82$ for the system at $z = 1.581$ and $\log(N/\text{cm}^2) > 14.91$ for the one at $z = 1.444$. Both values can only be considered as an upper limit since the feature is clearly saturated in both cases. We tentatively detect two possible absorption features at the corresponding wavelength for C IV at $z = 1.663$, however, we cannot securely confirm these lines.

3.3 A hostless burst?

We do not find any source at the GRB 160410A position in our late GTC/OSIRIS image (right panel of Fig. 2, [Fong et al. 2022](#) also do not detect the host in other filters to shallower limits). We obtain a limiting magnitude of $r' > 27.17 \text{ mag}$ (AB, corrected for Galactic extinction), which corresponds to an absolute magnitude limit of $M_{r'} > -18.44 \text{ mag}$. None of the nearby sources in the field are likely to be the possible host of GRB 160410A. The closest object is at a projected distance of $r \sim 4''.9$ from the GRB position which

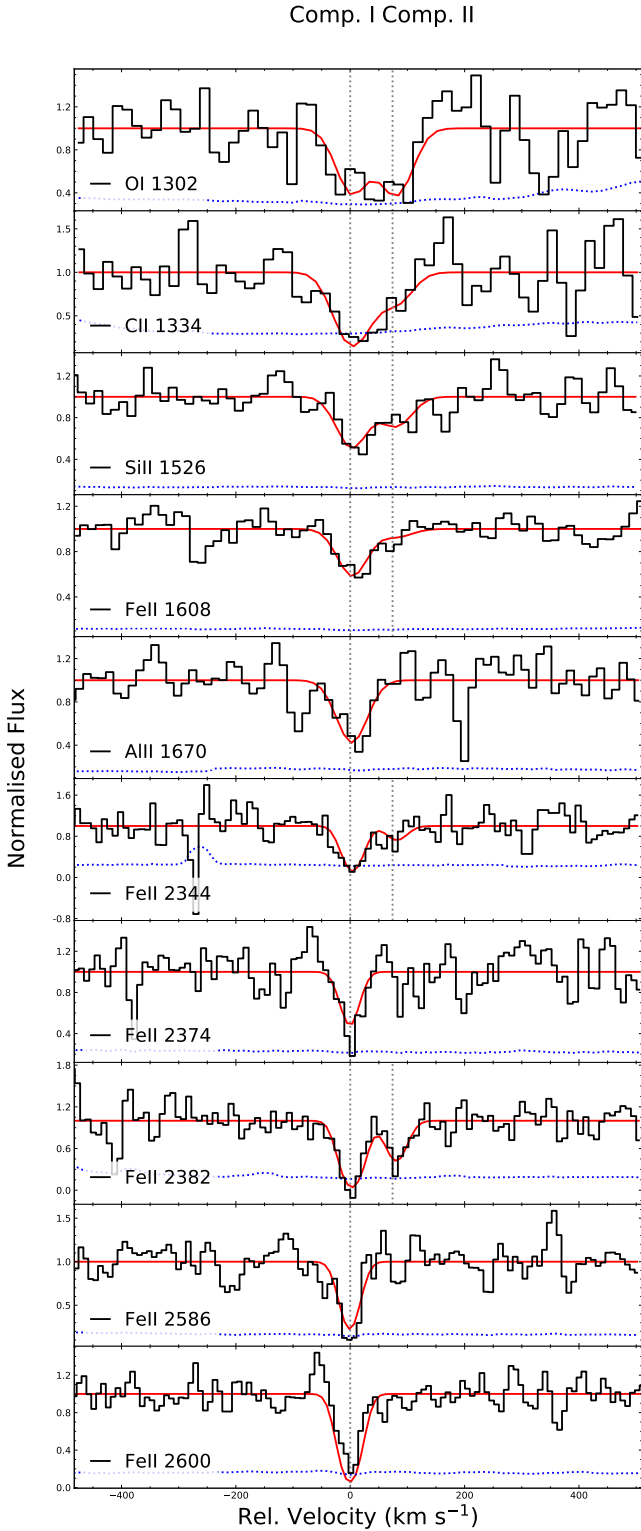


Figure 3. Absorption features detected in the GRB 160410A afterglow emission as observed in the X-shooter afterglow spectrum. Black lines correspond to the normalised spectrum in velocity space, centered at the redshift of the GRB. We also plot the error spectrum for each line (blue dotted line) and in vertical grey we mark the components listed in Tab. 2. The red solid line shows the Voigt best-fit profile for each absorption feature.

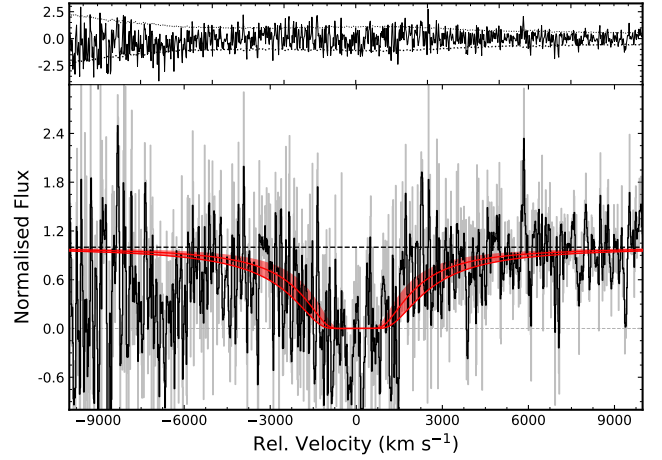


Figure 4. Voigt profile fitting of the Ly α absorption line. The top panel shows the residuals and the 1σ error spectrum (dotted line). In the bottom panel we plot the spectrum smoothed with a Gaussian kernel of 2σ in black and the original, non-smoothed, spectrum in grey. The red solid line represents the best-fit Voigt profile. For clarity, we show in shaded red the corresponding errors.

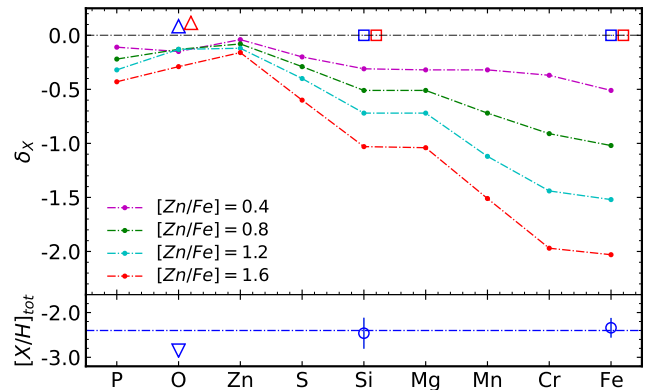


Figure 5. Dust depletion pattern and metallicity for the measured column densities of the features found in absorption in the afterglow of GRB 160410A. *Top panel:* Dust depletion sequence for GRB 160410A. Squares (top panel) and circles (bottom panel) denote the Si and Fe lines meanwhile triangles refer to the limits we derive for the saturated O line. Red squares denote the depletion δ_X values obtained for the common velocity component to all the elements observed, blue squares are the depletion considering the total column density measured. For comparison, we plot with a dash-dotted line in different colours the dust depletion sequence obtained from the fitting of QSO-DLA absorption systems in De Cia et al. (2016). *Bottom panel:* Corresponding metallicity for the observed ions considering all the velocity components. The mean metallicity is shown with a dashed-dotted line.

translates to a distance⁷ of ~ 42 kiloparsecs. The host galaxy is also not detected at $3.6 \mu\text{m}$ in our deep *Spitzer*/IRAC observations. Following the methods of Perley et al. (2016a,b), combined with the significantly deeper optical upper limit, this yields an upper limit on the stellar mass of $M_* \lesssim 1.14 \times 10^9 M_\odot$.

⁷ We made use of the astropy packages SkyCoord and Cosmology.

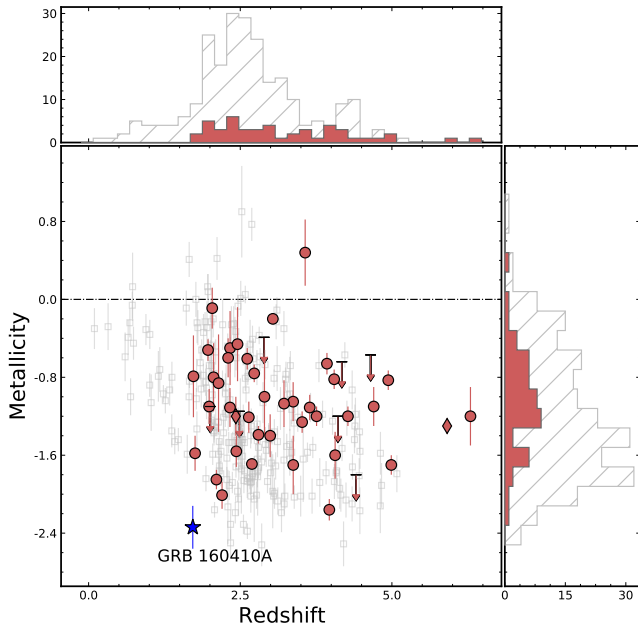


Figure 6. Metallicity of GRB host galaxies and QSO-DLAs vs. redshift. *Middle panel:* Clear grey empty squares mark QSO-DLAs from the sample published in [De Cia et al. \(2018\)](#). Red filled circles show the metallicities for long GRB-DLAs and a red filled diamond marks sub-DLA systems. Most of the data are from [Thöne et al. \(2013\)](#). We note that these values are not dust-corrected. We add some more recent metallicity values from the literature ([de Ugarte Postigo et al. 2018](#); [Krühler et al. 2013](#); [Friis et al. 2015](#); [Heintz et al. 2018](#), and J. Greiner, priv. comm.). The values from [de Ugarte Postigo et al. \(2018\)](#) and [Heintz et al. \(2018\)](#) are dust-corrected following [De Cia et al. \(2016\)](#). The value from [Friis et al. \(2015\)](#) is dust-corrected following [De Cia et al. \(2013\)](#). We also show the distribution of metallicities on the right and the distribution in redshift on the top. Hatched histograms show QSO-DLAs, red filled values show the long GRB-DLA sample. While QSO-DLA metallicities are based only on Fe and dust-corrected, the GRB-DLA metallicities are based on several elements such as Sulfur, Silicon, Zinc, Iron and Oxygen and are, generally, not dust-corrected

. As GRB 160410A is a completely new class in itself, we do not show it in the histograms.

Given our upper limit on the host stellar mass we compare our results to the mass-metallicity relation (MZR) following the equations presented in [Ma et al. \(2016\)](#). The low Fe-based (see Sect. 3.2.2) metallicity value would imply a stellar mass of $\log(M_*/M_\odot) = 6.18 \pm 0.52$. This value indicates a low stellar mass for the host galaxy of GRB 160401A. This together with the deep limits in r -band and $3.6 \mu\text{m}$ (see Sect. 2.4.2) is telling us that the host galaxy for GRB 160410A must be very faint

We compare our host galaxy limit to other, securely associated, long and short GRB hosts from the literature. For short GRBs, we use the sample from [Leibler & Berger \(2010\)](#) and [O'Connor et al. \(2022\)](#), for long GRB hosts we use the SHOALS sample ([Perley et al. 2016a](#), D. A. Perley, S. Schulze, priv. comm.). We selected only those GRB hosts with detections or upper limits in the r' and R_C bands. In Fig. 10 we see that, for short GRBs, the associated hosts have a broad distribution in brightness. Note, however, that only three SGRBs have a spectroscopically confirmed redshift from absorption lines in their GRB afterglow, whereas the rest get their redshifts from the associated host galaxies. At the same time, SGRBs at redshifts beyond $z \sim 1$ are very sparse, hence we have to be aware

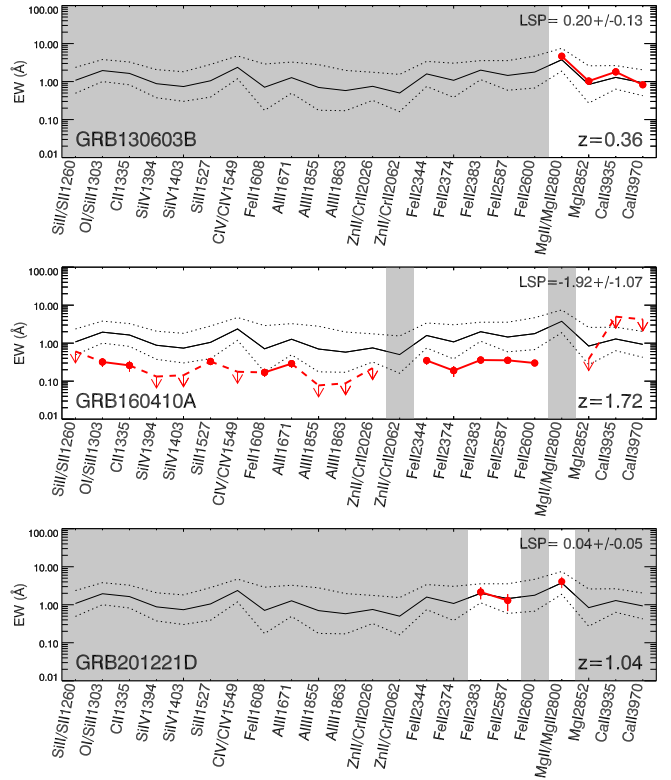


Figure 7. Equivalent width diagrams for the GRB 130603B ([de Ugarte Postigo et al. 2014a](#)), GRB 160410A and GRB 201221D afterglow spectra and GRB 201221D spectrum following the process described in [de Ugarte Postigo et al. \(2012\)](#). Red dots denote the corresponding EW for the absorption lines detected, whereas the red triangles show an inferred upper limit. The black solid line marks the average of the sample used in [de Ugarte Postigo et al. \(2012\)](#) and the upper and lower dotted lines show the standard deviation. Grey areas represent no detection of the corresponding spectral features is possible.

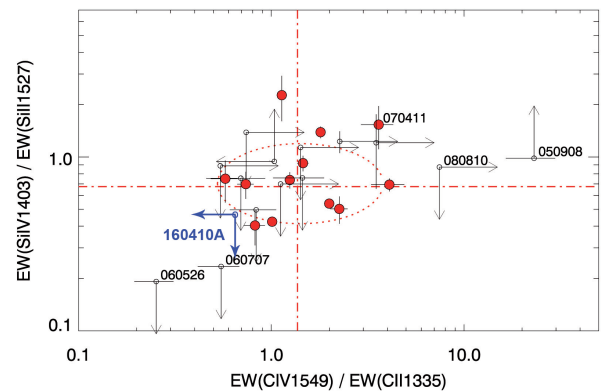


Figure 8. High-/low-ionisation C and Si line EW ratio comparison for GRB 160410A (*in blue*) compared with the sample of and using the method presented in [de Ugarte Postigo et al. \(2012\)](#). The red filled dots mark the ratio for detections in the afterglow spectroscopy of long GRBs, empty dots with arrows show upper limits in one or both ratios. The red dash-dotted lines represent the average values of the sample, the ellipse marks the 1σ region.

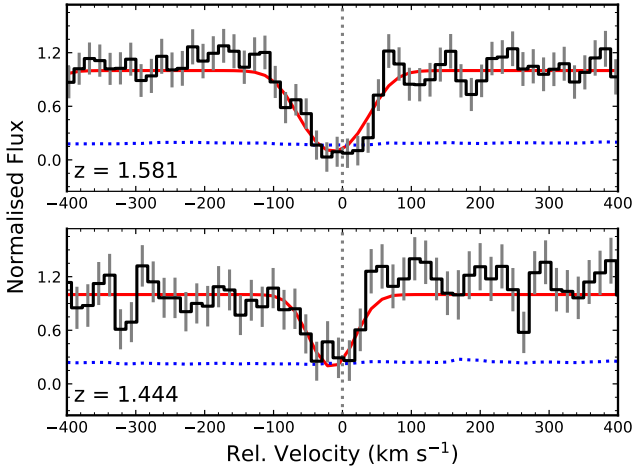


Figure 9. Absorption features detected along the line-of-sight towards GRB 160410A for the two intervening systems. *Top:* C IV ($\lambda\lambda 1550\text{\AA}$) line at $z = 1.581$. *Bottom:* Absorption line corresponding to C IV ($\lambda\lambda 1550\text{\AA}$) at $z = 1.444$. See the caption of Fig. 3 concerning the colour coding. The vertical dotted grey line is the fitted broad component at $v = 0 \text{ km s}^{-1}$. We see that the minimum of the Voigt best-fit profile, in both cases, is clearly shifted to the left due to the lines being saturated.

of possible biases here, as had been found for LGRB hosts before the presentation of unbiased samples (see e.g. Perley et al. 2016a,b). However, we can conclude that any host of GRB 160410A would be at the faint end of the distribution, even compared to long GRB hosts.

The photometric observations alone, without spectroscopic confirmation of the redshift, could have led us to think that GRB 160410A belonged to the class of hostless SGRBs. However, the presence of a DLA as well as the metallic absorption features are indicative of the burst being hosted by a galaxy.

3.4 GRB 160410A afterglow light curve and its spectral energy distribution.

The light curve of the optical afterglow is described by a smoothly double-broken power-law, which yields a steep/shallow/steep decay with decay indices α_{steep} , α_{plateau} , and α_{late} , respectively, as well as two break times $t_{b,1}$, $t_{b,2}$. We find $\alpha_{\text{steep}} = 1.11 \pm 0.17$, $\alpha_{\text{plateau}} = 0.19 \pm 0.04$, $t_{b,1} = 0.0052 \pm 0.0030 \text{ d}$ ($446 \pm 256 \text{ s}$); and $\alpha_{\text{late}} = 1.86 \pm 0.18$, $t_{b,2} = 0.162 \pm 0.030 \text{ d}$. The break sharpness was fixed to sharp values ($n = -10, 10$ respectively), and the host galaxy was neglected, as we find no evidence for any host down to very deep limits (Sect. 3.3). We show the optical afterglow of GRB 160410A in Fig. 11, including the best-fit triple power-law.

We use the fit to construct the Spectral Energy Distribution (SED), which stretches from $uvw1$ to z' . We fit the SED with both a simple power-law (no dust) and dust models for Milky Way (MW), Large (LMC), and Small Magellanic Cloud (SMC) dust (Pei 1992). Therefore, we exclude the $uvw1$ and u bands as these lie blueward and within Ly α respectively. The SED and the fits are shown in Fig. 12.

For no extinction, we find $\beta = 0.46 \pm 0.25$, and a fit with $\chi^2/\text{d.o.f.} = 0.19$. For the three dust models, we find: MW dust: $\beta = 0.30 \pm 0.35$, $A_V = 0.14 \pm 0.22 \text{ mag}$; LMC dust: $\beta = -0.18 \pm 1.21$, $A_V = 0.34 \pm 0.63 \text{ mag}$; and SMC dust: $\beta = 2.55 \pm 2.81$, $A_V = -0.74 \pm 0.99 \text{ mag}$. All these fits are show over-fitting ($\chi^2/\text{d.o.f.}$ from 0.06 to 0.16). However, the SMC fit is clearly unphysical (yielding

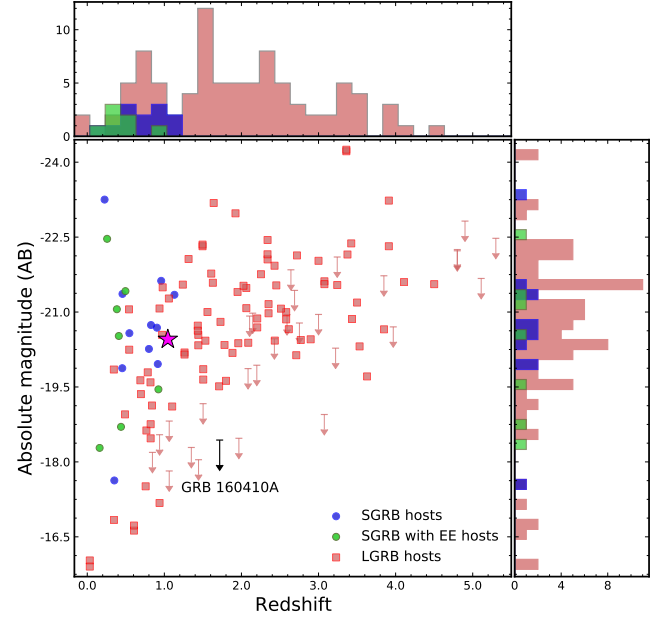


Figure 10. Long GRB host magnitudes in the r' and R_C bands from the SHOALS sample (D. A. Perley, S. Schulze, priv. comm.). For SGRB hosts, we take r' and R magnitudes from Leibler & Berger (2010) and O'Connor et al. (2022) when available. The sample is the same one utilized in the “Amati” relation (see Sect. 4.1). Note that we are using a fixed (observer-frame) band-pass filter despite a wide redshift distribution, hence the actual rest-frame band would be blue-shifted by $(1+z)$. For clarity, we plot r' and R_C with the same colour. On top and left-most we show the distribution in redshift and absolute magnitude, respectively, for each sample. In blue, we show the SGRB hosts, in clear green the SGRB with EE hosts and in clear red, the distribution for long GRB hosts. The GRB 160410A upper limit is plotted with a black arrow and GRB 201221D, with a magenta star. All the absolute magnitudes are corrected for Galactic extinction (Schlafly & Finkbeiner 2011).

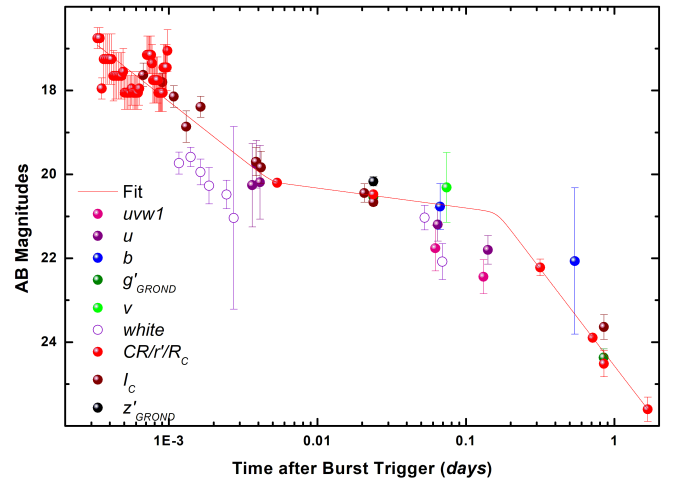


Figure 11. Light curve of the GRB 160410A afterglow. For reasons of clarity, upper limits are omitted. Early I_C data are from Trotter et al. (2016), the R_C data point at 0.31 d is from Wang et al. (2016), the rest from this work. Data are in the AB magnitude system and corrected for Galactic foreground extinction. The red line show the modelled light curve for the $CR/r'/R_C$ -band. A clear steep-shallow-plateau-steep transition is visible.

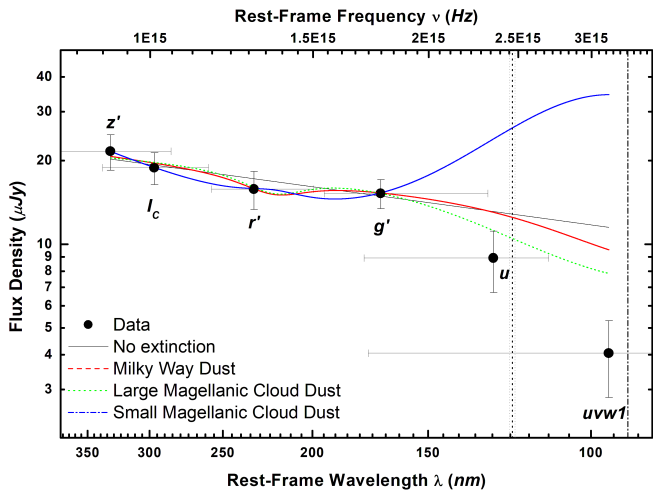


Figure 12. Spectral Energy Distribution of the afterglow of GRB 160410A. Flux densities are determined at break time, 0.162 d. Horizontal error bars represent filter widths, these errors were not included in the fits. We show fits with no extinction (straight black line), Milky-Way dust (red dashed line), Large-Magellanic-Cloud dust (green dotted line), and Small-Magellanic-Cloud dust (blue dash-dotted line). The SMC fit is clearly unphysical, and the results of the LMC fit also show it is not realistic, see Sect. 3.4. The MW is possible, but a fit with no extinction is the preferred model. The u and $uvw1$ data points were excluded from the fit as they are affected by $\text{Ly}\alpha$ and Lyman forest/limit absorption. The $\text{Ly}\alpha$ wavelength at the redshift of the GRB is marked by a vertical dotted line, with the adjacent dotted gray lines marking the FWHM of the $\text{Ly}\alpha$ line. A dash-dotted vertical line marks the Lyman cutoff.

negative extinction, i.e. emissive dust), and the negative intrinsic spectral slope for LMC dust is also not expected for GRB afterglows. Only the MW fit yields a sensible result, however, dust extinction is 0 within errors, so we find no evidence for dust and hence continue to work with the no-extinction fit. The no-extinction model is also the one showing the least overfitting.

To compare this high-redshift SGRB afterglow with other SGRBs, we take SGRBs with redshifts and well-detected afterglows (as well as the deep upper limits of GRB 050509B) from the sample of [Kann et al. \(2011\)](#) (there called “Type I GRBs”), and provide additional analysis for four further SGRBs (one with an unsure classification) in Appendix B. We show the observed (corrected for Galactic foreground extinction and, if needed, host-galaxy contribution) light curves in the Appendix, in Fig. B1.

GRB 160410A lies at a higher redshift than any of these events except for GRB 181123B, which lies at a slightly higher redshift. Knowing the redshift and SED, we use the method of [Kann et al. \(2006\)](#) to shift all afterglows to a common redshift of $z = 1$, corrected for dust extinction (see Fig. 13). The afterglow of GRB 180418A is the brightest SGRB afterglow at very early times, but not far above that of GRB 160410A. During the plateau phase, the afterglow of GRB 160410A has a similar luminosity as that of the extremely intense GRB 090510. At later times, the very extended plateau of the GRB 150424A afterglow makes it brighter than GRB 160410A at the same time. Due to their (relatively) high redshifts and brightness at early times the nature of GRBs 160410A and 180418A have been heavily discussed (see also Sect. 4). However, at 12 h post burst, both afterglows still lie among the faintest LGRB afterglows, which is further evidence that these are likely true SGRBs.

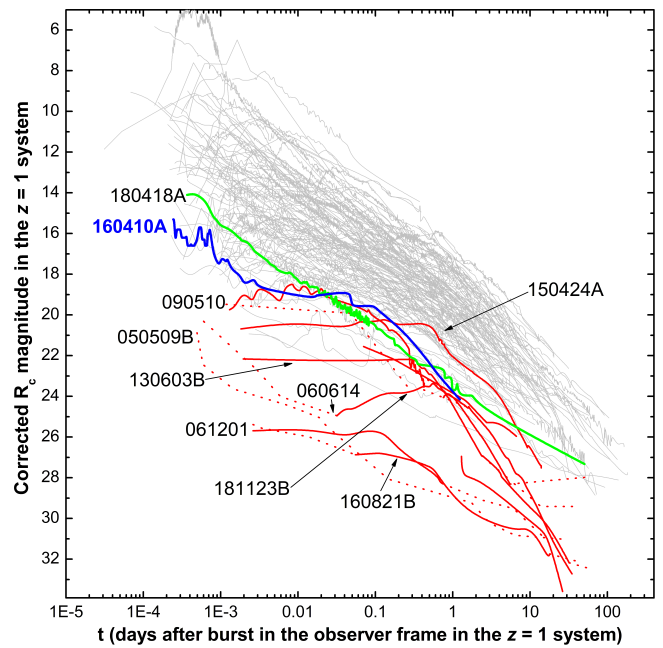


Figure 13. Afterglow of GRB 160410A (thick blue line) in the context of a large sample of GRB afterglows. Thin grey lines are afterglows of long GRBs. Thicker red lines are a selection of afterglows of other SGRBs. GRB 180418A (green line) has an insecure classification. The afterglows are given in the $z = 1$ system, see text for more details.

3.5 The GRB 201221D spectra

This is the only SGRB since GRB 160410A for which we were able to detect absorption lines in the spectrum, albeit with a low S/N. The GRB afterglow is detected in the acquisition image with a magnitude of $r' = 23.95 \pm 0.20$ mag, calibrated using five Pan-STARRS field stars and not corrected for Galactic extinction ([Schlafly & Finkbeiner 2011](#)). In the GRB 201221D spectrum, we find up to four absorption lines that we interpret as due to the Mg II doublet and to Fe II lines. In addition, we also observe $[\text{O II}]\lambda 3727$ in emission from the host. The emission falls within a telluric band and its detection tells us that the emission must therefore be rather strong (see [de Ugarte Postigo et al. 2020](#)). All the features are at a redshift of $z = 1.0450 \pm 0.0008$, making GRB 201221D another high-redshift SGRB and, in this case, with a clearly star-forming host galaxy. The spectrum is shown in Fig. 14.

We measure EWs in the spectrum using the [GRBSpec](#) database and compare it to the sample of long GRBs ([de Ugarte Postigo et al. 2012](#)) in Fig. 7. In this case, the strength of the absorption features is consistent with the average for long GRBs ($\text{LSP} = 0.04 \pm 0.05$) in contrast to GRB 160410A where the lines were much weaker. Due to the wavelength coverage, we cannot detect the high ionisation absorption lines of Si IV and C IV and hence cannot come to a conclusion on the ionisation of the ISM. In any case, the r' -band value measured for the GRB afterglow is consistent within errors with the one for the host galaxy (see Tab.3) and therefore, continuum contamination from the host galaxy is present in our spectrum. Thus, the EW/LSP measures might be contaminated and are not fully comparable to GRB 160410A and GRB 130603B.

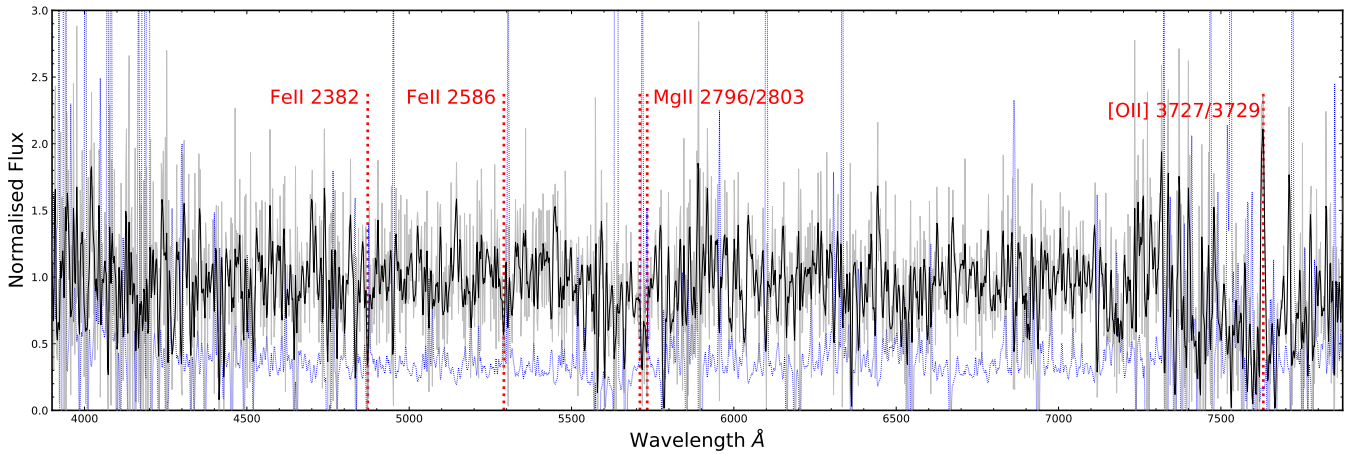


Figure 14. GTC/OSIRIS spectrum of the afterglow emission of GRB 201221D. For plotting reasons, we smooth the spectrum by applying a Gaussian kernel of 1σ to the data. The colour coding is the same one as used in Fig. 1. We add the non-smoothed spectrum (grey) in the background.

Table 3. Photometry of the GRB 201221D host galaxy. Data are given in AB magnitudes and are corrected for Galactic foreground extinction (Schlafly & Finkbeiner 2011).

Time after burst (days)	Magnitude (AB)	Exposure Time (s)	Band	Instrument
19.349	23.80 ± 0.12	120	g'	LBC
19.349	23.83 ± 0.15	120	r'	LBC
19.349	23.44 ± 0.18	120	i'	LBC
19.349	23.11 ± 0.25	120	z'	LBC
13.879	22.40 ± 0.17	60	J	LUCIFER
13.895	22.15 ± 0.20	60	K_S	LUCIFER

3.6 The host of GRB 201221D

In contrast to GRB 160410A we do find a faint host candidate for GRB 201221D at the same position as the GRB. The photometry of the host candidate is shown in Tab. 3 for all the bands observed with the LBT telescope. We analyse the Spectral Energy Distribution (SED) of the host galaxy with the available photometry using CIGALE⁸ (Burgarella et al. 2005; Noll et al. 2009; Boquien et al. 2019) in its most recent version. We apply a delayed star-formation history with an age for the main stellar population varying freely from 1.0 Gyr to 13 Gyr and a more recent burst whose age varies from 20 Myr to 1 Gyr. The Initial Mass Function (IMF) we use is described in Chabrier (2003) with a Bruzual & Charlot (2003) stellar population model, assuming a metallicity (Z) of 0.008, 0.02 or 0.05 (where $Z = 0.02$ is Solar metallicity Bruzual & Charlot 2003).

The dust attenuation is modeled with the modified attenuation law described in Calzetti et al. (2000) as implemented in CIGALE (see Sect. 3.4.2 in Boquien et al. 2019). We consider a Milky Way (MW) (Cardelli et al. 1989) extinction model with a $R_V = 3.1$ and a colour excess in the nebular lines starting in 0.1 and then, varying in steps of 0.05 between 0.05 and 1.0. We also considered a Small Magellanic Cloud (SMC) and a Large Magellanic Cloud (LMC) (Pei 1992)

⁸ <https://cigale.lam.fr/>

Table 4. Properties of the putative host galaxy of GRB 201221D.

Property	Value
A_V (mag)	0.56 ± 0.34
Z	0.02
$\log_{10}(M) (M_{\odot})$	$9.79^{+0.13}_{-0.19}$
$\log_{10}(SFR) (M_{\odot}/yr)$	$0.81^{+0.19}_{-0.33}$
$sSFR (Gyr^{-1})$	1.06 ± 0.67
Reduced χ^2	0.45

extinction model but in both cases, the model was unsatisfactory compared to the one performed considering a MW model. We also allow the attenuation curve slope to vary from -0.4 to 0.4 , changing it in steps of 0.2 (see Eq. 8 in Boquien et al. 2019). For the re-emitted energy from dust heated by stellar photons, we use the models from Dale et al. (2014) and let α_{IR} , the exponent of the radiation field intensity distribution (Dale & Helou 2002), vary between 1.0, 2.0 or 3.0.

We find a best fit to the SED using a model galaxy spectrum with an intermediate mass and a moderate star-formation rate (SFR), as well as a low specific star-formation rate (sSFR). However, our modelling shows some degree of over-fitting, which might be due to the low number of data points. The results for the SED modeling are listed in Tab. 4 and a figure of the best model can be seen in Appendix D.

4 DISCUSSION

4.1 On the short/long nature of GRB 160410A

Ever since the discovery of a bimodal distribution of GRB prompt emission light curves both in the temporal range (Mazets et al. 1981) as well as the spectral hardness (Kouveliotou et al. 1993), methods to discern between “long/soft” and “short/hard” GRBs have been extensively discussed in the literature (see e.g. Lü et al. 2010, 2014; Tsutsui et al. 2013; Shahmoradi & Nemiroff 2015; Zhang et al. 2016, 2018; Li et al. 2016, 2020; Jespersen et al. 2020, for some works on this topic). Here we will study GRB 160410A with several classification methods to derive clues on its nature.

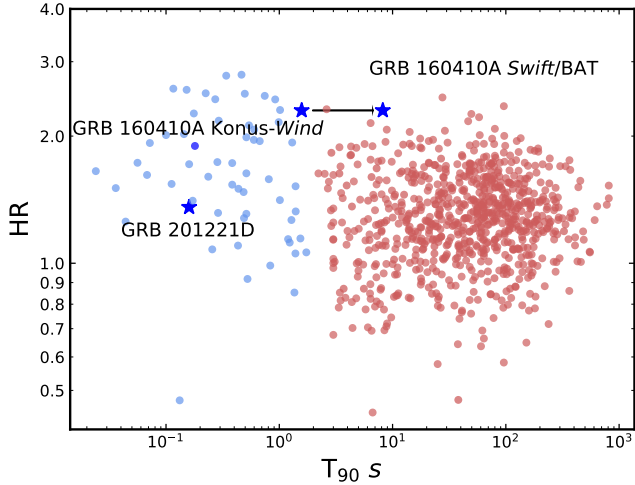


Figure 15. Hardness Ratio (HR) vs. duration T_{90} using data from Lien et al. (2016). Based on the work from Kouveliotou et al. (1993), we show SGRBs in blue and long GRBs in red. The hardness ratio of GRB 201221D is marked with a blue star as derived from the *Swift*/BAT data products (https://gcn.gsfc.nasa.gov/notices_s/682269/BA/). For GRB 160410A we plot the HR derived in Dichiara et al. (2021) with the T_{90} from *Swift*/BAT on top right and T_{90} derived for the initial peak complex from Konus-Wind data (Minaev & Pozanenko 2020) on top left.

Tsutsui et al. (2013) first found significant statistical evidence for an “Amati” relation between the isotropic energy release E_{iso} and the rest-frame peak energy of the prompt emission spectrum E_{peak} , rest-frame long known for long GRBs (Amati et al. 2002; Amati 2006), for SGRBs parallel to that of long GRBs but offset by a factor of ~ 100 . Using a significantly increased sample, Minaev & Pozanenko (2020, 2021, henceforth MP20) confirm this result, and GRB 160410A fits with the Amati relation for SGRBs (Fig. 16)⁹. Furthermore, MP20 introduce two classifiers, EH and EHD (Energy-Hardness and Energy-Hardness-Duration, respectively). They find that GRB 160410A is in full agreement with the high values found for other short GRBs.

To confirm the results of MP20, we gathered GRB energetics, mostly from Tsvetkova et al. (2017, 2021) and compute the isotropic energy¹⁰. The final sample is shown in Fig. 16 and we perform a simple fitting to the two GRB classes following Eq. 1 as presented in MP20.

$$\log\left(\frac{E_{\text{peak}}}{100 \text{ keV}}\right) = a \cdot \log\left(\frac{E_{\text{iso}}}{10^{51} \text{ erg}}\right) + b \quad (1)$$

For SGRBs we found a slope of $a_{\text{short}} = 0.30$ and $b_{\text{short}} = 0.78$ with a standard deviation of $\sigma_{\text{short}} = 0.05$ and $R^2 = 0.50$, for long GRBs the slope is $a_{\text{long}} = 0.33$, $b_{\text{long}} = -0.01$ with a $\sigma_{\text{long}} = 0.02$ and $R^2 = 0.52$. We do not perform a more extended fitting as it is done in MP20 since it is not the aim of the present paper.

Another classification distinction is the *hardness ratio* (HR), which

⁹ Note the Amati relation is also a powerful tool for the opposite case, such as the recently reported GRB 200826A (Rossi et al. 2022; Ahumada et al. 2021; Zhang et al. 2021), which was temporally short but fully in agreement with the long-GRB Amati relation and was shown to be accompanied by a supernova.

¹⁰ https://github.com/steveschulze/GRB_Eiso.git

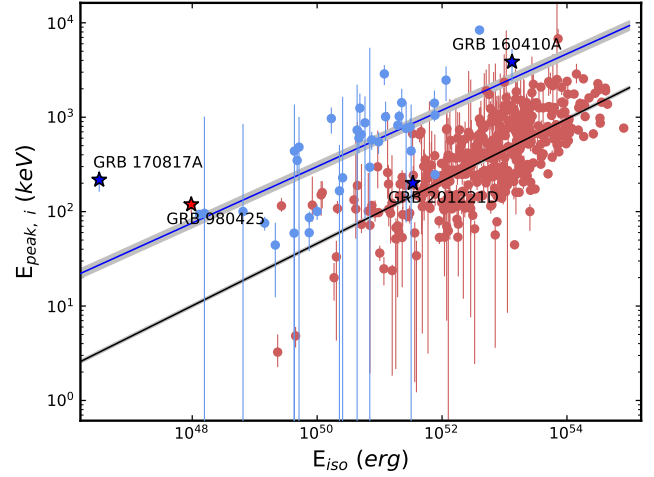


Figure 16. Modified version of the Amati relation. We highlight the positions of GRB 160410A and GRB 201221D with blue stars, as derived from the Konus-Wind published data, see Sect. 4.1. SGRBs are plotted in blue, long GRBs in red. In the corresponding colours, the best linear fits are plotted together with a shaded area around them marking the 1σ region for each fit. Here we do not distinguish between SGRBs and SGRBs with extended emission.

is the ratio of the fluence in the 50–100 keV band over the 25–50 keV band. Dichiara et al. (2021) obtained a $HR = 2.3 \pm 0.5$ for the main spike and claim GRB 160410A is a short GRB with extended emission. GRB 160410A can be classified as a long GRB (see Fig. 15), if we only consider the T_{90} as the classification criterion. However, if we consider the initial peak complex and GRB 160410A as a short GRB with EE, as in Dichiara et al. (2021), we see that it matches with the short GRB scheme.

Kann et al. (2011) compare the afterglows of SGRBs to a large sample of those of long GRBs. They find $\overline{M_B} = -23.14 \pm 0.17$ mag (FWHM 1.61 mag) for long GRB afterglows at one day in the $z = 1$ frame, and $\overline{M_B} = -17.34 \pm 0.50$ mag (FWHM 1.65 mag) for the short GRB afterglows at the same time. For GRB 160410A, we derive $M_B = -19.04$ mag from our fit to the late-time light curve. This places the absolute magnitude of the afterglow at the upper edge of the FWHM of the SGRB afterglow absolute magnitude distribution, but 2.5 mag below that of long GRB afterglows, making it more likely that GRB 160410A is a short GRB.

Further classifiers in the context of GRB 160410A can be found in Appendix A. With a few exceptions, these find that GRB 160410A is a genuine SGRB, or at least more likely to be one than a long GRB. We therefore conclude that GRB 160410A has evidence showing it to be a member of the SGRB population.

The other SGRB studied here, GRB 201221D, actually matches very well the location for long GRBs in the Amati relation (see Fig. 16). However, its shortness and hardness (see Sect. 2.5 and Fig. 15) put this GRB clearly within the SGRB category.

4.2 The GRB 160410A environment in the context of long GRBs and short GRBs

The sample of short GRBs with detected absorption lines in its spectrum is still very small: GRB 130603B (de Ugarte Postigo et al. 2014a), GRB 160410A, and GRB 201221D (both in this study). GRB 160410A is the only one that allows a chemical study of the

gas in the host to be performed, as it has been commonly done for long GRBs (see e.g. [de Ugarte Postigo et al. 2018](#); [Krühler et al. 2013](#); [Heintz et al. 2018](#)). The spectrum shows features common to long GRBs such as Fe II, Al II or Si II; however, it does not show any high ionisation lines of Si IV nor C IV, which are usually detected in long GRB environments (see e.g. [Vreeswijk et al. 2004](#); [Christensen et al. 2011](#); [de Ugarte Postigo et al. 2012](#); [Heintz et al. 2018](#)). [Cao et al. \(2016\)](#) report the detection of C IV lines in their afterglow spectrum together with the Mg II $\lambda\lambda 2796, 2803$ doublet, which, however, happens to fall within the telluric A-band.

Despite the scarcity of currently available SGRB afterglow spectra, it seems that SGRB sight-lines show a large diversity, as it is the case for their host galaxies. The spectra of all three SGRBs with absorption line spectra cover the Mg II and the Fe II lines as common features. GRB 201221D and GRB 130603B show the Mg II $\lambda 2796, 2803$ doublet, while the Fe II lines are only present in GRB 201221D. In GRB 160410A we do not observe Ca II or Na I detected in GRB 130603B. However, we detect a large number of additional absorption lines that were out of the observable range in the other two SGRBs due to their lower redshift. There is also a tentative detection of Ni II but the significance is very low.

GRB 130603B happened in a spiral galaxy in what appears to be a tidally disrupted arm ([de Ugarte Postigo et al. 2014a](#)). In the spectrum of GRB 201221D we detect [O II] $\lambda 3727$ emission lines, implying the presence of an underlying star-forming host galaxy. Furthermore, both we and multiple other observing teams ([Dichiara et al. 2020](#); [Kilpatrick et al. 2020](#); [Rastinejad et al. 2020](#); [Dimple et al. 2020](#)) report the detection of a faint extended source at the afterglow position. The host of GRB 201221D (see Sect. 3.6) is a massive galaxy consistent with the common value found in prior works on SGRB hosts (see e.g. [Leibler & Berger 2010](#)). The star-formation rate is also in agreement with the values found for SGRB hosts ([Berger 2009](#)).

For GRB 160410A, however, we found no host galaxy down to very deep limits (see Sect. 3.3) and we find no hint of emission lines in the NIR. In contrast, the detection of the broad Ly α absorption line and the large column density tell us that the GRB happened within or behind a DLA, which are usually associated with a galaxy (see e.g. [Wolfe et al. 2005](#); [Christensen et al. 2014](#)). This implies that there must be an underlying galaxy for GRB 160410A but it might be very faint. It is also possible that the progenitor system of GRB 160410A has been kicked out from its host and merged outside the host or in the halo. The fact that we detect a DLA in the sight-line implies that the GRB still has to be well within the H I halo of the galaxy. Given the high redshift of the system and typical kick velocities, a binary NS-NS system could move tens of kiloparsecs away from the host galaxy beyond the extension of hydrogen of the galaxy ([Mandhai et al. 2022](#)). The distance in projection to the closest observable galaxy in the GRB 160410A field is ~ 42 kpc (under the assumption this galaxy is at the redshift of GRB 160410A), making it very unlikely to be the host of the GRB while observing such a large neutral hydrogen column density and many other absorption lines.

In prior works, the detection of the highly ionized C IV and Si IV absorption lines has been assumed to originate in the hot gas of the galactic halo of DLAs (see e.g. [Ledoux et al. 1998](#); [Wolfe & Prochaska 2000](#); [Maller et al. 2003](#); [Fox et al. 2008](#); [Heintz et al. 2018](#)). The detection of a DLA system and the non-detection of these lines in the GRB 160410A afterglow spectrum would hence not favour this GRB to be in the halo or it would imply that the host has no hot gas halo.

Our analysis shows that the environment of GRB 160410A is very

different from the ones measured in the case of long GRB hosts. The probed material has a very low ionisation and very weak lines in general (see Sect. 3.2.3). In contrast, GRB 201221D (see Sect. 3.5) and GRB 130603B show LSPs of 0.04 ± 0.05 and 0.20 ± 0.13 , respectively, very close to the average value for long GRB sight-lines ([de Ugarte Postigo et al. 2012](#)). A high LSP value typically points toward an environment highly ionised due to star-formation and, conversely, a low value pinpoints the opposite. For long GRBs, the LSPs are usually high since these are commonly associated with star-forming environments. The SGRBs 130603B and 201221D occurred within their hosts galaxies; however, for GRB 160410A, no underlying galaxy was detected. We see in Fig. 7 that, whereas for GRBs 130603B and 201221D the EW profiles follow the average one of long GRBs. However, we note that for GRB 201221D, EW values might be contaminated by the host continuum (see Sect. 3.5) and, therefore, the LSP. GRB 160410A is completely different compared to either long GRBs or to the other two SGRBs with detected features in their afterglows. With a significantly lower value for the LSP and the non-detection of an underlying galaxy, GRB 160410A seems to have happened in an environment that is not actively forming stars.

Furthermore, the measured [Si/Fe] ratio between an α -element such Si, that is produced in core-collapse SNe, and the detection of Fe, mostly produced in Type Ia SNe, might be indicating that there is no α -enhancement and therefore the absence of recent star formation in the host galaxy, which is consistent with the non detection of the galaxy, the low ionisation and the low metallicity of the traced gas (see e.g. [Wiersma et al. \(2009\)](#); [Vargas et al. \(2013\)](#)).

In line with those observations, the metallicity of the material observed along the sight-line is very low (Sect. 3.2.2), comparable to the lowest values for QSO absorbers (see e.g. [De Cia et al. \(2018\)](#) and Fig. 6). Compared to galaxies in the local Universe, the metallicity is higher but inline with values obtained for e.g. Tucana II, an UFD galaxy with a metallicity of [Fe/H] ~ -3.0 ([Ji et al. 2016b](#)). Note, however, that this metallicity was determined from four stars, neither the ISM nor the CGM. This would further support the idea of an underlying very faint host galaxy for GRB 160410A, however, the average metallicity of galaxies at $z \sim 1.7$ is also lower than in the local Universe.

The fact that we have a low metallicity environment and possibly a very faint host galaxy contradicts general expectations for the environment of short GRBs. If the absorption lines are weak because we have an evolved galaxy with an old population that has exhausted most of the gas, we would expect a high metallicity. However, if the progenitor BNS had been kicked out from its host we should expect a low metallicity. Also [Zhang et al. \(2009\)](#) assume in their classification scheme of short vs. long GRBs that SGRB hosts have a high metallicity (see also [Li et al. 2020](#)). The only two other GRBs with absorption line spectroscopy and hence secure host galaxy associations do seem to be different from GRB 160410A, showing much stronger lines and luminous hosts.

The question is whether SGRBs with EE might have somewhat different progenitors and in consequence different hosts or environments. The list of SGRBs with EE is rather short (see e.g. [Lien et al. 2016](#)) and only a few of them have an associated host galaxy. [Minaev & Pozanenko \(2020\)](#) list eleven events as SGRBs with EE (GRBs 050709, 050724, 060614, 061006, 061210, 070714B, 071227, 080123, 110402A, 150424A and 160410A). We compare the derived host properties from the GRB afterglow spectrum of GRB 160410A as well as from the field observation with *Spitzer*/IRAC with SGRBs with EE and an associated host galaxy (see Fig. 10). There is no difference in the distribution of absolute magnitudes between the hosts of normal SGRBs and those with EE,

the slight shift towards lower redshifts might be an observational issue since higher redshifts make the detection of the lower luminosity EE more challenging. Taking the stellar masses obtained by SED modeling from Nugent et al. (2020) for those seven SGRB showing EE (GRBs 050709, 050724, 061006, 061210, 070714B, 071227 and 080123, Minaev & Pozanenko 2020), we see that their masses are typically larger than the upper limit we obtain from the *Spitzer* observations (see Sect. 3.3), although a few have stellar masses lower than our limit for the host of GRB 160410A. A more recent and complete study on one SGRB with EE, GRB 050709, shows a low-luminosity host, a subsolar metallicity and a low SFR (Nicuesa Guelbenzu et al. 2021), which would be all in line with what we see for GRB 160410A. A more recent case is GRB 181123B, a SGRB with EE and an associated star-forming and massive host at $z = 1.754$ (see Paterson et al. 2020; Dichiaro et al. 2021). Its association with the galaxy is still under debate (Rowlinson et al. 2021). However, in Rastinejad et al. (2022), the properties of the associated host galaxy of GRB 211211A are in line with the limits for the host of GRB 160410A. Despite its prompt emission shape and duration, GRB 211211A is claimed to be a SGRB with EE and the associated host galaxy seems to be a galaxy with a low stellar mass and a low SFR.

It would be important to settle the issue of the host galaxy association by deep imaging with e.g. the Hubble Space Telescope (HST) or the James Webb Space Telescope (JWST), to determine the nature of the host and the location of the GRB within it to understand why we observe this peculiar environment in this burst.

SGRBs have also been proposed to happen within galaxy clusters (see e.g. Berger 2010), so that could be a possible explanation for the absence of detection of a host for GRB 160410A. However, again, the large column density of neutral hydrogen goes against this hypothesis as DLAs are commonly associated with galaxies, as mentioned before. We also do not see a very crowded field in Fig. 2.

DLA systems found in QSO absorbers have been associated with the halo of galaxies (Wolfe et al. 2005). The non-detection of an underlying galaxy and the fact that the closest possible galaxy is at 42 kpc from the GRB location could also mean that the GRB itself happened at a large distance from its host and that the lines we see in the afterglow spectrum are actually an intervening system. However, the non-detection of the GRB afterglow in the $uvw2$ and $uvm2$ bands and the detection in the $uvw1$ band (see Sect. 2 and Appendix C) establish a redshift upper limit for the GRB afterglow using the Lyman “drop-out” technique of $z = 1.8$. This points to an association of the afterglow with the ISM detected at the absorption line redshift, making it unlikely that the DLA belongs to a foreground galaxy.

5 CONCLUSIONS

In this paper, we present the first study of the ISM of a SGRB host galaxy. The burst itself was one of the hardest and brightest events ever detected and at the highest redshift ever measured directly from its afterglow spectrum (and not from the association with a potential host galaxy). The X-shooter spectrum shows a broad H I absorption with a large column density consistent with being a DLA. We derive a very low metallicity of $[\text{Fe}/\text{H}] = -2.5$, one of the lowest (dust-depletion corrected) value ever measured. GRB 160410A shows a very low ionisation compared to what is commonly found for the environments of LGRBs. SED fitting to the light curve of the afterglow and dust depletion analysis from absorption lines finds no indication for dust extinction along the sight-line. We do not find any host galaxy down to a very deep limit; however, the presence of the

DLA system in the burst afterglow spectrum indicates that there has to be an underlying host.

The GRB 160410A afterglow seems to be rather different compared to the other two SGRB afterglows with detected absorption lines, being significantly brighter than any other SGRB afterglow at very early times except for the controversial case of GRB 180418A (note both early detections were obtained with TAROT). GRB 201221D is located within a more massive, star-forming ionised host galaxy, consistent with previous findings for SGRB hosts. However, our spectral coverage does not allow us to determine its metallicity. The spectrum of GRB 160410A was obtained less than ten minutes after the GRB alert and has the largest sample of lines observed in a short GRB afterglow spectrum. This demonstrates the importance of the rapid response mode for observing these events. More data sets of this quality are needed to obtain more robust statistical conclusions on the ISM and environments of SGRBs.

ACKNOWLEDGEMENTS

JFAF acknowledges support from the Spanish Ministerio de Ciencia, Innovación y Universidades through the grant PRE2018-086507. DAK and JFAF acknowledge support from Spanish National Research Project RTI2018-098104-J-I00 (GRBPhot). AdUP acknowledges funding from a Ramón y Cajal fellowship (RyC-2012-09975). MB acknowledges funding associated to a personal tecnico de apoyos fellowship (PTA2016-13192-I). DBM acknowledges research grant 19054 from VILLUM FONDEN. Part of the funding for GROND (both hardware as well as personnel) was generously granted from the Leibniz Prize to Prof. G. Hasinger (DFG grant HA 1850/28-1). A. R. acknowledges support from the INAF project Premiale Supporto Arizona & Italia.

This work is partly based on observations made with the Gran Telescopio Canarias (GTC), installed in the Spanish Observatorio del Roque de los Muchachos of the Instituto de Astrofísica de Canarias, in the island of La Palma. Partly based on observations made with the Nordic Optical Telescope, owned in collaboration by the University of Turku and Aarhus University, and operated jointly by Aarhus University, the University of Turku and the University of Oslo, representing Denmark, Finland and Norway, the University of Iceland and Stockholm University at the Observatorio del Roque de los Muchachos, La Palma, Spain, of the Instituto de Astrofísica de Canarias. Partly based on observations made with the Large Binocular Telescope (LBT). The LBT is an international collaboration among institutions in the United States, Italy and Germany. LBT Corporation partners are: The University of Arizona on behalf of the Arizona Board of Regents; Istituto Nazionale di Astrofisica, Italy; LBT Beteiligungsgesellschaft, Germany, representing the Max-Planck Society, The Leibniz Institute for Astrophysics Potsdam, and Heidelberg University; The Ohio State University, representing OSU, University of Notre Dame, University of Minnesota and University of Virginia.

This work made use of the GRBspec database <https://grbspec.eu>. This work has made extensive use of IRAF and Python, particularly with *astropy* (<http://www.astropy.org>, Astropy Collaboration et al. 2013, 2018), *matplotlib* (Hunter 2007), *photutils* (Bradley et al. 2020) and *numpy* (Harris et al. 2020).

DATA AVAILABILITY

The spectroscopic data shown in this paper are publicly available in the GRBSpec database, at <http://grbspec.eu>. Raw imaging data are available in the observatory archives (ESO - Science Archive Facility, GTC Public Archive, Spitzer Heritage Archive (SHA), *Swift* Archive). Data non-publicly available on observatory archives, as well as reduced imaging data will be delivered on reasonable request to the corresponding author.

REFERENCES

- Abbott B. P., et al., 2017a, *ApJ*, **848**, L12
- Abbott B. P., et al., 2017b, *ApJ*, **848**, L13
- Acciari V. A., et al., 2021, *ApJ*, **908**, 90
- Ackermann M., et al., 2010, *ApJ*, **716**, 1178
- Ahumada T., et al., 2021, *Nature Astronomy*, **5**, 917
- Alam S., et al., 2015, *ApJS*, **219**, 12
- Amati L., 2006, *MNRAS*, **372**, 233
- Amati L., et al., 2002, *A&A*, **390**, 81
- Anderson G. E., et al., 2021, *MNRAS*, **503**, 4372
- Andreoni I., et al., 2021, *ApJ*, **918**, 63
- Antier S., et al., 2020, *MNRAS*, **497**, 5518
- Aptekar R. L., et al., 1995, *Space Sci. Rev.*, **71**, 265
- Astropy Collaboration et al., 2013, *A&A*, **558**, A33
- Astropy Collaboration et al., 2018, *AJ*, **156**, 123
- Barthelmy S. D., et al., 2005, *Space Sci. Rev.*, **120**, 143
- Becerra R. L., et al., 2019, *ApJ*, **881**, 12
- Belczynski K., Perna R., Bulik T., Kalogera V., Ivanova N., Lamb D. Q., 2006, *ApJ*, **648**, 1110
- Bellm E. C., et al., 2019, *PASP*, **131**, 018002
- Beniamini P., Piran T., 2019, *MNRAS*, **487**, 4847
- Beniamini P., Nava L., Duran R. B., Piran T., 2015, *MNRAS*, **454**, 1073
- Beniamini P., Hotokezaka K., Piran T., 2016a, *ApJ*, **829**, L13
- Beniamini P., Hotokezaka K., Piran T., 2016b, *ApJ*, **832**, 149
- Berger E., 2009, *ApJ*, **690**, 231
- Berger E., 2010, *ApJ*, **722**, 1946
- Berger E., 2014, *ARA&A*, **52**, 43
- Berger E., Fong W., Chornock R., 2013, *ApJ*, **774**, L23
- Blažek M., de Ugarte Postigo A., Kann D. A., Thöne C. C., Agüí Fernández J. F., Izzo L., 2020, in Society of Photo-Optical Instrumentation Engineers (SPIE) Conference Series. p. 1145218, [doi:10.1117/12.2562420](https://doi.org/10.1117/12.2562420)
- Bolmer J., et al., 2019, *A&A*, **623**, A43
- Boquien M., Burgarella D., Roehly Y., Buat V., Ciesla L., Corre D., Inoue A. K., Salas H., 2019, *A&A*, **622**, A103
- Bradley L., et al., 2020, *astropy/photutils*: 1.0.0, [doi:10.5281/zenodo.4044744](https://doi.org/10.5281/zenodo.4044744), <https://doi.org/10.5281/zenodo.4044744>
- Breeveld A. A., Siegel M. H., 2016, GRB Coordinates Network, **19839**
- Breeveld A. A., Landsman W., Holland S. T., Roming P., Kuin N. P. M., Page M. J., 2011, in J. E. McEnery, J. L. Racusin, & N. Gehrels ed., American Institute of Physics Conference Series Vol. 1358, American Institute of Physics Conference Series. pp 373–376 ([arXiv:1102.4717](https://arxiv.org/abs/1102.4717)), [doi:10.1063/1.3621807](https://doi.org/10.1063/1.3621807)
- Bruzual G., Charlot S., 2003, *MNRAS*, **344**, 1000
- Burgarella D., Buat V., Iglesias-Páramo J., 2005, *MNRAS*, **360**, 1413
- Burrows D. N., et al., 2005, *Space Sci. Rev.*, **120**, 165
- Butler N., et al., 2015, GRB Coordinates Network, **17762**
- Calzetti D., Armus L., Bohlin R. C., Kinney A. L., Koornneef J., Storchi-Bergmann T., 2000, *ApJ*, **533**, 682
- Cano Z., Wang S.-Q., Dai Z.-G., Wu X.-F., 2017, *Advances in Astronomy*, **2017**, 8929054
- Cao Y., Kulkarni S. R., Yan L., Ravi V., Vedantham H. K., Kasliwal M. M., 2016, GRB Coordinates Network, **19278**
- Cardelli J. A., Clayton G. C., Mathis J. S., 1989, *ApJ*, **345**, 245
- Chabrier G., 2003, *PASP*, **115**, 763
- Choi C., Kim Y., Park W., Shin S., Im M., 2018, GRB Coordinates Network, **22668**
- Christensen L., Fynbo J. P. U., Prochaska J. X., Thöne C. C., de Ugarte Postigo A., Jakobsson P., 2011, *ApJ*, **727**, 73
- Christensen L., Møller P., Fynbo J. P. U., Zafar T., 2014, *MNRAS*, **445**, 225
- Cobb B. E., 2016, GRB Coordinates Network, **19311**
- Cucchiara A., et al., 2013, *ApJ*, **777**, 94
- D’Elia V., et al., 2009a, *A&A*, **503**, 437
- D’Elia V., et al., 2009b, *ApJ*, **694**, 332
- Dale D. A., Helou G., 2002, *ApJ*, **576**, 159
- Dale D. A., Helou G., Magdis G. E., Armus L., Díaz-Santos T., Shi Y., 2014, *ApJ*, **784**, 83
- De Cia A., Ledoux C., Savaglio S., Schady P., Vreeswijk P. M., 2013, *A&A*, **560**, A88
- De Cia A., Ledoux C., Mattsson L., Petitjean P., Srianand R., Gavignaud I., Jenkins E. B., 2016, *A&A*, **596**, A97
- De Cia A., Ledoux C., Petitjean P., Savaglio S., 2018, *A&A*, **611**, A76
- Dichiara S., Troja E., Cenko S. B., O’Connor B., Gatkine P., Durbak J. M., Kutuyev A., Veilleux S., 2020, GRB Coordinates Network, **29128**
- Dichiara S., et al., 2021, *ApJ*, **911**, L28
- Dimple A., Panchal A., Gangopadhyay A., Ghosh A., Gupta R., Kumar A., Misra K., Pandey S. B., 2020, GRB Coordinates Network, **29148**
- Fong W., Berger E., 2013, *ApJ*, **776**, 18
- Fong W., et al., 2014, *ApJ*, **780**, 118
- Fong W.-f., et al., 2022, *ApJ*, **940**, 56
- Fontana A., et al., 2014, *A&A*, **570**, A11
- Fox A. J., Ledoux C., Vreeswijk P. M., Smette A., Jaunsen A. O., 2008, *A&A*, **491**, 189
- Frederiks D., et al., 2016, GRB Coordinates Network, **19288**
- Frederiks D., et al., 2020, GRB Coordinates Network, **29130**
- Freudling W., Romaniello M., Bramich D. M., Ballester P., Forchi V., García-Dabó C. E., Moehler S., Neeser M. J., 2013, *A&A*, **559**, A96
- Friis M., et al., 2015, *MNRAS*, **451**, 167
- Fruchter A. S., et al., 2006, *Nature*, **441**, 463
- Fynbo J. P. U., Prochaska J. X., Sommer-Larsen J., Dessauges-Zavadsky M., Møller P., 2008, *ApJ*, **683**, 321
- Gaia Collaboration et al., 2018, *A&A*, **616**, A1
- Galama T. J., et al., 1998, *Nature*, **395**, 670
- Gatkine P., Veilleux S., Cucchiara A., 2019, *ApJ*, **884**, 66
- Gehrels N., et al., 2004, *ApJ*, **611**, 1005
- Gehrels N., et al., 2006, *Nature*, **444**, 1044
- Giallongo E., et al., 2008, *A&A*, **482**, 349
- Gibson S. L., Malesani D., Page K. L., Palmer D. M., Siegel M. H., 2016, GRB Coordinates Network, **19271**
- Goldstein A., et al., 2017, *ApJ*, **848**, L14
- Gompertz B. P., et al., 2022, *Nature Astronomy*, **2022**, 1000000
- Gonneau A., et al., 2020, *A&A*, **634**, A133
- Graham M. J., et al., 2019, *PASP*, **131**, 078001
- Greiner J., 2019, *PASP*, **131**, 015002
- Greiner J., et al., 2008, *PASP*, **120**, 405
- Guidorzi C., Martone R., Kobayashi S., Mundell C. G., Gomboc A., Steele I. A., 2018, GRB Coordinates Network, **22648**
- Hamburg R., Malacaria C., Meegan C., Fermi GBM Team 2020, GRB Coordinates Network, **29140**
- Hamuy M., Suntzeff N. B., Heathcote S. R., Walker A. R., Gigoux P., Phillips M. M., 1994, *PASP*, **106**, 566
- Harris C. R., et al., 2020, *Nature*, **585**, 357
- Heintz K. E., et al., 2018, *MNRAS*, **479**, 3456
- Hjorth J., Bloom J. S., 2012, The Gamma-Ray Burst - Supernova Connection. pp 169–190
- Hjorth J., et al., 2003, *Nature*, **423**, 847
- Horiuchi T., Hanayama H., Honma M., Itoh R., Shiraishi K., Murata K., Tachibana Y., Kawai N., 2018, GRB Coordinates Network, **22670**
- Horne K., 1986, *PASP*, **98**, 609
- Hunter J. D., 2007, *Computing in Science & Engineering*, **9**, 90
- Jakobsson P., et al., 2006, *A&A*, **460**, L13
- Japelj J., et al., 2015, *A&A*, **579**, A74

- Jespersen C. K., Severin J. B., Steinhardt C. L., Vinther J., Fynbo J. P. U., Selsing J., Watson D., 2020, *ApJ*, **896**, L20
- Ji A. P., Frebel A., Chiti A., Simon J. D., 2016a, *Nature*, **531**, 610
- Ji A. P., Frebel A., Ezzeddine R., Casey A. R., 2016b, *ApJ*, **832**, L3
- Jin Z.-P., et al., 2018, *ApJ*, **857**, 128
- Juvan I., et al., 2016, GRB Coordinates Network, 19309
- Kann D. A., Klose S., Zeh A., 2006, *ApJ*, **641**, 993
- Kann D. A., et al., 2011, *ApJ*, **734**, 96
- Kann D. A., Tanga M., Greiner J., 2015, GRB Coordinates Network, 17757
- Kasliwal M. M., Korobkin O., Lau R. M., Wollaeger R., Fryer C. L., 2017, *ApJ*, **843**, L34
- Kilpatrick C. D., Malesani D. B., Fong W., 2020, GRB Coordinates Network, 29133
- Klose S., et al., 2019, *ApJ*, **887**, 206
- Klotz A., Gendre B., Stratta G., Atteia J. L., Boër M., Malacrino F., Damerdjij Y., Behrend R., 2006, *A&A*, **451**, L39
- Klotz A., Turpin D., Atteia J. L., Boer M., Laugier R., Gendre B., 2016, GRB Coordinates Network, 19287
- Knuist F., et al., 2017, *A&A*, **607**, A84
- Kouveliotou C., Meegan C. A., Fishman G. J., Bhat N. P., Briggs M. S., Koshut T. M., Paciesas W. S., Pendleton G. N., 1993, *ApJ*, **413**, L101
- Krimm H. A., et al., 2020, GRB Coordinates Network, 29139
- Krogager J.-K., 2018, VoigtFit: A Python package for Voigt profile fitting ([arXiv:1803.01187](https://arxiv.org/abs/1803.01187))
- Krühler T., et al., 2008, *ApJ*, **685**, 376
- Krühler T., et al., 2013, *A&A*, **557**, A18
- Kuin N. P. M., Swift/UVOT Team 2019, GRB Coordinates Network, 26538
- Lamb G. P., et al., 2019, *ApJ*, **883**, 48
- Ledoux C., Petitjean P., Bergeron J., Wampler E. J., Srianand R., 1998, *A&A*, **337**, 51
- Leibler C. N., Berger E., 2010, *ApJ*, **725**, 1202
- Li Y., Zhang B., Lü H.-J., 2016, *ApJS*, **227**, 7
- Li Y., Zhang B., Yuan Q., 2020, *ApJ*, **897**, 154
- Lien A., et al., 2016, *ApJ*, **829**, 7
- Lodders K., Palme H., Gail H. P., 2009, *Landolt & Bornstein*, **4B**, 712
- Lü H.-J., Liang E.-W., Zhang B.-B., Zhang B., 2010, *ApJ*, **725**, 1965
- Lü H.-J., Zhang B., Liang E.-W., Zhang B.-B., Sakamoto T., 2014, *MNRAS*, **442**, 1922
- Lyman J. D., et al., 2017, *MNRAS*, **467**, 1795
- Ma X., Hopkins P. F., Faucher-Giguère C.-A., Zolman N., Muratov A. L., Kereš D., Quataert E., 2016, *MNRAS*, **456**, 2140
- Malesani D., Kirkpatrick C., 2016, GRB Coordinates Network, 19295
- Malesani D., Xu D., Watson D. J., Blay P., 2015, GRB Coordinates Network, 17756
- Malesani D., Xu D., Kuutma T., 2016, GRB Coordinates Network, 19300
- Malesani D., Heintz K. E., Stone M., Stone J., 2018, GRB Coordinates Network, 22660
- Maller A. H., Prochaska J. X., Somerville R. S., Primack J. R., 2003, *MNRAS*, **343**, 268
- Mandhai S., Lamb G. P., Tanvir N. R., Bray J., Nixon C. J., Eyles-Ferris R. A. J., Levan A. J., Gompertz B. P., 2022, *MNRAS*, **514**, 2716
- Marshall F. E., Gibson S. L., 2016, GRB Coordinates Network, 19275
- Mazets E. P., et al., 1981, *Ap&SS*, **80**, 3
- Meegan C., et al., 2009, *ApJ*, **702**, 791
- Metzger B. D., 2019, *Living Reviews in Relativity*, **23**, 1
- Metzger B. D., et al., 2010, *MNRAS*, **406**, 2650
- Minaev P. Y., Pozanenko A. S., 2020, *MNRAS*, **492**, 1919
- Minaev P. Y., Pozanenko A. S., 2021, *MNRAS*, **504**, 926
- Misra K., Paswan A., Singh M., Pandey S. B., Kumar T. S., Omar A., 2018, GRB Coordinates Network, 22663
- Modigliani A., et al., 2010, in *Observatory Operations: Strategies, Processes, and Systems III*. p. 773728, [doi:10.1117/12.857211](https://doi.org/10.1117/12.857211)
- Muraki Y., et al., 2016, GRB Coordinates Network, 19285
- Nicuesa Guelbenzu A. M., et al., 2021, *A&A*, **650**, A117
- Noll S., Burgarella D., Giovannoli E., Buat V., Marcellac D., Muñoz-Mateos J. C., 2009, *A&A*, **507**, 1793
- Norris J. P., Bonnell J. T., 2006, *ApJ*, **643**, 266
- Nugent A. E., et al., 2020, *ApJ*, **904**, 52
- O'Connor B., et al., 2022, *MNRAS*, **515**, 4890
- Oates S. R., et al., 2009, *MNRAS*, **395**, 490
- Oke J. B., 1990, *AJ*, **99**, 1621
- Page K. L., et al., 2020, GRB Coordinates Network, 29112
- Pandey S. B., et al., 2019, *MNRAS*, **485**, 5294
- Paterson K., et al., 2020, *ApJ*, **898**, L32
- Pei Y. C., 1992, *ApJ*, **395**, 130
- Perley D. A., et al., 2016a, *ApJ*, **817**, 7
- Perley D. A., et al., 2016b, *ApJ*, **817**, 8
- Planck Collaboration et al., 2014, *A&A*, **571**, A16
- Poole T. S., et al., 2008, *MNRAS*, **383**, 627
- Prochaska J. X., Chen H.-W., Dessauges-Zavadsky M., Bloom J. S., 2007, *ApJ*, **666**, 267
- Rastinejad J., Paterson K., Kilpatrick C. D., Fong W., 2020, GRB Coordinates Network, 29142
- Rastinejad J. C., et al., 2021, *ApJ*, **916**, 89
- Rastinejad J. C., et al., 2022, *Nature*, **612**, 223
- Roederer I. U., et al., 2016, *AJ*, **151**, 82
- Roming P. W. A., et al., 2005, *Space Sci. Rev.*, **120**, 95
- Rossi A., CIBO Collaboration 2021, GRB Coordinates Network, 29311
- Rossi A., et al., 2022, *ApJ*, **932**, 1
- Rouco Escorial A., et al., 2021, *ApJ*, **912**, 95
- Rowlinson A., et al., 2021, *MNRAS*, **506**, 5268
- Sakamoto T., et al., 2016, GRB Coordinates Network, 19276
- Savchenko V., et al., 2017, *ApJ*, **848**, L15
- Schady P., 2018, GRB Coordinates Network, 22662
- Schady P., Chen T. W., 2018, GRB Coordinates Network, 22666
- Schlafly E. F., Finkbeiner D. P., 2011, *ApJ*, **737**, 103
- Seifert W., et al., 2003, in Iye M., Moorwood A. F. M., eds, *Society of Photo-Optical Instrumentation Engineers (SPIE) Conference Series Vol. 4841, Instrument Design and Performance for Optical/Infrared Ground-based Telescopes*. pp 962–973, [doi:10.1117/12.459494](https://doi.org/10.1117/12.459494)
- Selsing J., et al., 2016, GRB Coordinates Network, 19274
- Selsing J., et al., 2019, *A&A*, **623**, A92
- Shahmoradi A., Nemiroff R. J., 2015, *MNRAS*, **451**, 126
- Skrutskie M. F., et al., 2006, *AJ*, **131**, 1163
- Starling R. L. C., Willingale R., Tanvir N. R., Scott A. E., Wiersema K., O'Brien P. T., Levan A. J., Stewart G. C., 2013, *MNRAS*, **431**, 3159
- Tanvir N. R., Levan A. J., Fruchter A. S., Hjorth J., Hounsell R. A., Wiersema K., Tunnicliffe R. L., 2013, *Nature*, **500**, 547
- Tanvir N. R., et al., 2017, *ApJ*, **848**, L27
- Tanvir N. R., et al., 2019, *MNRAS*, **483**, 5380
- Thöne C. C., et al., 2008, *ApJ*, **676**, 1151
- Thöne C. C., et al., 2013, *MNRAS*, **428**, 3590
- Tody D., 1993, in Hanisch R. J., Brissenden R. J. V., Barnes J., eds, *Astronomical Society of the Pacific Conference Series Vol. 52, Astronomical Data Analysis Software and Systems II*. p. 173
- Troja E., et al., 2018, GRB Coordinates Network, 22664
- Troja E., et al., 2019, *MNRAS*, **489**, 2104
- Troja E., et al., 2022, *Nature*, **612**, 228
- Trotter A., et al., 2016, GRB Coordinates Network, 19277
- Tsutsui R., Yonetoku D., Nakamura T., Takahashi K., Morihara Y., 2013, *MNRAS*, **431**, 1398
- Tsvetkova A., et al., 2017, *ApJ*, **850**, 161
- Tsvetkova A., et al., 2021, *ApJ*, **908**, 83
- Udike A. C., et al., 2008, *ApJ*, **685**, 361
- Vargas L. C., Geha M., Kirby E. N., Simon J. D., 2013, *ApJ*, **767**, 134
- Vernet J., et al., 2010, in *Ground-based and Airborne Instrumentation for Astronomy III*. p. 77351I, [doi:10.1117/12.857124](https://doi.org/10.1117/12.857124)
- Vernet J., et al., 2011, *A&A*, **536**, A105
- Vreeswijk P. M., et al., 2004, *A&A*, **419**, 927
- Vreeswijk P. M., et al., 2007, *A&A*, **468**, 83
- Vreeswijk P. M., et al., 2011, *A&A*, **532**, C3
- Wang C. J., Mao J., Bai J. M., 2016, GRB Coordinates Network, 19280
- Watson D., et al., 2019, *Nature*, **574**, 497
- Wiersma R. P. C., Schaye J., Theuns T., Dalla Vecchia C., Tornatore L., 2009, *MNRAS*, **399**, 574
- Wolfe A. M., Prochaska J. X., 2000, *ApJ*, **545**, 591

- Wolfe A. M., Gawiser E., Prochaska J. X., 2005, *ARA&A*, **43**, 861
- Woodsley S. E., Bloom J. S., 2006, *ARA&A*, **44**, 507
- Yang J., et al., 2022, *Nature*, **612**, 232
- Yates R., Kruehler T., Greiner J., 2016, GRB Coordinates Network, 19272
- Yoldaş A. K., Krühler T., Greiner J., Yoldaş A., Clemens C., Szokoly G., Primak N., Klose S., 2008, in Galassi M., Palmer D., Fenimore E., eds, American Institute of Physics Conference Series Vol. 1000, Gamma-ray Bursts 2007. pp 227–231, doi:10.1063/1.2943450
- Zhang B., 2006, *Nature*, **444**, 1010
- Zhang B., et al., 2009, *ApJ*, **703**, 1696
- Zhang Z.-B., Yang E.-B., Choi C.-S., Chang H.-Y., 2016, *MNRAS*, **462**, 3243
- Zhang Z. B., Zhang C. T., Zhao Y. X., Luo J. J., Jiang L. Y., Wang X. L., Han X. L., Terheide R. K., 2018, *PASP*, **130**, 054202
- Zhang B. B., et al., 2021, *Nature Astronomy*, **5**, 911
- de Ugarte Postigo A., et al., 2012, *A&A*, **548**, A11
- de Ugarte Postigo A., et al., 2014a, *A&A*, **563**, A62
- de Ugarte Postigo A., Blazek M., Janout P., Sprimont P., Thöne C. C., Gorosabel J., Sánchez-Ramírez R., 2014b, in Software and Cyberinfrastructure for Astronomy III. p. 91520B, doi:10.1117/12.2055774
- de Ugarte Postigo A., et al., 2018, *A&A*, **620**, A119
- de Ugarte Postigo A., Kann D. A., Izzo L., Thoene C. C., Blazek M., Agui Fernandez J. F., Lombardi G., 2020, GRB Coordinates Network, 29132
- van Dokkum P. G., 2001, *PASP*, **113**, 1420

APPENDIX A: FURTHER ANALYSIS OF THE SHORT/LONG NATURE OF GRB 160410A

Further to the analysis of the Amati relation and the hardness ratio presented in Sect. 4.1, we here detail an extended study of the short/long GRB nature of GRB 160410A.

Zhang et al. (2009) introduced the “Type I” and “Type II” classification scheme, independent of the classic T_{90} division, which was originally motivated by the temporally long, peculiar GRB 060614 (Gehrels et al. 2006; Zhang 2006). Type II GRBs are those associated with the core-collapse of massive stars (so usually long and soft), whereas Type I GRBs are those that are not - usually short and hard GRBs, which are at least in part associated with the merger of compact objects, specifically inspiralling binary neutron stars (e.g. Abbott et al. 2017a,b).

We follow figure 8 of Zhang et al. (2009) to derive a classification for GRB 160410A in the Type I/II scheme. The GRB has (as measured by *Swift*) a $T_{90} > 2$ s, and also a $T_{90}/(1+z) > 2$ s. However, it shows a short “Initial Pulse Complex” followed by an “Extended Emission” bump, which is an often-seen feature of Type I GRBs (Norris & Bonnell 2006). In Fig. A1 we show the *Swift*/BAT light curve obtained by the analysis of the *Swift*/BAT Gamma-Ray Burst Catalogue¹¹.

There is no information on any supernova (SN) contribution as the redshift is too high, nor are we aware of any late-time follow-up. Similarly, there is little information on the host galaxy as it is not detected even in our very deep late-time follow-up. Further decisions in the decision tree also cannot be answered with certainty, until the last step.

The bolometric isotropic energy release for this GRB is $\log E_{\gamma}/\text{erg} = 53.1$, certainly not a low value, strictly leading to an “unknown” classification. However, we note the extremely energetic GRB 090510 which has a similar isotropic energy release¹² is

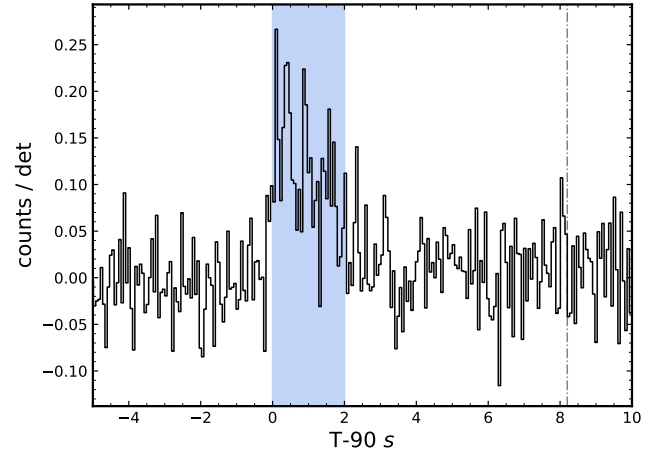


Figure A1. BAT mask-weighted lightcurve in the 15 to 350 keV range of GRB 160410A with 64 ms binning. The blue area marks a multi-peaked structure during the first two seconds. The dash-dotted line marks the end of the T_{90} duration from Sakamoto et al. (2016) in the same energy band.

also categorised as a short GRB (Ackermann et al. 2010; Kann et al. 2011). Therefore, using this scheme, we classify GRB 160410A as a Type I candidate.

Lü et al. (2010) devise a new parameter $\epsilon(\kappa) \equiv E_{\gamma,\text{iso},52}/E_{p,z,2}^{\kappa}$ with $E_{\gamma,\text{iso},52}$ being the bolometric isotropic energy release in units of 10^{52} erg, and $E_{p,z,2}^{\kappa}$ being the intrinsic peak energy in units of 10^2 keV. They find $\kappa = 5/3$ in their study. A study of GRBs with known parameters reveals four regions separated by low/high $T_{90,z}$ and low/high κ , the delineations being $\epsilon = 0.03$ ($\log \epsilon = -1.52$) and $T_{90,z} = 5$ s ($\log T_{90,z} = 0.26$). For the parameters given by Konus-Wind (Tsvetkova et al. 2017) we derive $E_{p,z} = 3853_{-973}^{+1429}$ keV and $E_{\gamma,\text{iso},52} = 13.21_{-0.68}^{+0.50}$. It is $T_{90,z} = 3.02 \pm 0.59$ s for *Swift* (with extended emission) and $T_{90,z} = 0.58 \pm 0.045$ s for Konus-Wind (only the initial pulse complex is detected). Using these values, we derive $\log \epsilon = -1.71$, which places it into the sector of Type I GRBs, though in the bottom left quadrant of Fig. 1 in Lü et al. (2010) and, within that sector, in the top right corner, close to the bulk of the Type I GRBs with EE. Only for the combination of lowest peak energy and highest isotropic energy release would it fall slightly into the sector of intrinsically short Type II GRBs.

Lü et al. (2014) discuss the “amplitude parameter” f which they define as the ratio between the 1 s peak count rate and the background count rate over the same time span. They simulate what f value will be derived for long GRBs when adding noise to the point that the $T_{90} < 2$ s, a value they designate as f_{eff} . They find f_{eff} values for such noised long GRBs have a mean value $\bar{f}_{\text{eff}} = 1.24$, whereas $f \gtrsim 2$ for Type I GRBs. For GRB 160410A, $f = 2.13$ is derived, with f_{eff} being essentially the same value as the extended emission is very faint (H.-J. Lü, priv. comm.). This indicates GRB 160410A is a true Type I GRB, but the evidence is marginal.

Li et al. (2020) create a method to use multiwavelength data to determine the probability whether a GRB is of Type I or Type II. This uses both prompt emission data as well as environment/host galaxy data (metallicity, offset, stellar mass). Their data collection is based on Li et al. (2016) which does not include GRB 160410A. We used

¹¹ <http://swift.gsfc.nasa.gov/results/batgrbcatalog>

¹² Tsutsui et al. (2013) argue the bolometric energy release for GRB 090510 should be measured in the 1 keV – 100 MeV energy frame, resulting from the extremely high peak energy. In this frame, $E_{\text{iso,bol}}$ is five times higher than in the usual frame and exceeds that of GRB 160410A.

their webpage¹³ to input all known parameters of GRB 160410A (the mean values as determined by Li et al. 2020 are used where we do not have information, such as on the host offset). Using all prompt-emission parameters and the upper limit on the host mass (see Sect. 3.3), we derive a 97% probability that this is a Type I GRB. However, if the extremely low metallicity is added, the probability switches completely, being vanishingly small for a Type I GRB. Considering all the other results in this section, this mainly points to the host environment of GRB 160410A being extreme within the known parameter range of Type I GRB host galaxies (likely coupled to the high redshift), in a way that is unaccounted for in the classifier.

From an analysis of large samples of long and short GRBs, Shammoradi & Nemiroff (2015) deduce the statistically most significant indicator of classification is E_p/T_{90} [keV, s⁻¹] (observer-frame values), with 99% of long GRBs having values ≤ 50 and 95% of short GRBs having values ≥ 50 . For GRB 160410A, we find $E_p/T_{90} = 173$ for the *Swift*-BAT T_{90} value, and $E_p/T_{90} = 893$ for the *Konus-Wind* duration, favoring that this is a short GRB.

Jespersen et al. (2020) present a method to classify GRBs based on prompt emission characteristics alone. They find that GRB 160410A is a long GRB. In their result table, they list the T_{90} duration to be 96 s, significantly in excess of the value of 8.2 s (Sakamoto et al. 2016). (We note that the *Swift* automatic BAT analysis page for this GRB¹⁴ even gives a value of ~ 320 s.) *Swift* entered the South Atlantic anomaly after several hundred seconds, which may influence the analysis and the significance of the Extended Emission. This, then, may also influence the classification of Jespersen et al. (2020) (C. K. Jespersen, priv. comm.).

APPENDIX B: ADDITIONAL TYPE I GRBS AND ANALYSIS

Further to several Type I GRBs taken from the sample of Kann et al. (2011), we include the following events for our comparison with GRB 160410A light curve:

B1 GRB 130603B

Data are taken from de Ugarte Postigo et al. (2014a); Pandey et al. (2019); Cucchiara et al. (2013); Berger et al. (2013). This bright Type I GRB is famous for showing the first clear evidence of a kilonova signature (Tanvir et al. 2013; Berger et al. 2013), having the first high S/N afterglow spectrum of a short GRB (de Ugarte Postigo et al. 2014a) and also showing clear evidence for a jet break (de Ugarte Postigo et al. 2014a; Fong et al. 2014). We fit the joint light curve with a smoothly broken power-law, finding $\alpha_1 = -0.24 \pm 0.20$, $\alpha_2 = 2.55 \pm 0.15$, $t_b = 0.281 \pm 0.028$ days. $n = 1$ has been fixed, and with the exception of UVOT *uvm2* and *u* data, the host galaxy has been subtracted by the authors of the data sources. We fit the SED (*uvm2*, *u*, *g'*, *V*, *r'*, *i'*, *z'*, *J*, *K*) with an intrinsic spectral slope of $\beta = 0.65$, following de Ugarte Postigo et al. (2014a), and find a large extinction $A_V = 0.84 \pm 0.11$ mag, in full agreement with de Ugarte Postigo et al. (2014a). Note that this is lower than the result found by Japelj et al. (2015), who find $A_V = 1.19^{+0.23}_{-0.12}$ mag, and SMC dust, albeit for a bluer spectral slope $\beta = 0.42^{+0.12}_{-0.22}$.

B2 GRB 150424A

Data are taken from Knust et al. (2017); Jin et al. (2018) as well as GCNs (Malesani et al. 2015; Butler et al. 2015). The redshift for this GRB is likely unknown, Klose et al. (2019) report spectroscopy of a nearby galaxy yields $z = 0.2981$, however, deep HST imaging reveals a faint extended red object under the afterglow, likely the host galaxy (Knust et al. 2017; Jin et al. 2018). Knust et al. (2017) estimate $z \approx 1$ from the afterglow SED, a value we adopt here.

We initially fit the afterglow with a broken power-law, and find $\alpha_1 = -0.01 \pm 0.03$, $\alpha_2 = 1.60 \pm 0.03$, $t_b = 0.396 \pm 0.017$ days, $n = 10$ has been fixed, and no host is included (the late HST data from Jin et al. 2018 are host-subtracted, and the host is very faint compared to the early data). However, this fit is statistically bad ($\chi^2/\text{d.o.f.} = 3.38$), and we find that especially the late-time HST data decay steeper than the extrapolation of the GROND data, which already indicates a steep decay, as initially reported by Kann et al. (2015). Using data only after the break ($t > 0.5$ days), and setting $J_G = F125W$, we find a best fit with another broken power-law $\alpha_{2,1} = 1.48 \pm 0.04$, $\alpha_{2,2} = 2.54 \pm 0.21$, $t_b = 4.139 \pm 0.739$ days, $n = 10$ fixed, no host. This is fully in agreement with the results of Jin et al. (2018). For this fit, the SED (g'_G , $F606W$, r'_G , i'_G , z'_G , J_G , $F160W$) is well-fit by a straight power-law with $\beta = 0.60 \pm 0.36$, in accordance with the value Jin et al. (2018) assumed. We note that the SED derived from our initial fit shows more scatter and a shallower slope, $\beta = 0.31 \pm 0.07$. Neither show evidence for extinction. As we assume $z = 1$, $dRc = 0$. Finally, we create a further SED by carefully aligning early UVOT data to the *white* “backbone”, and connecting that to late data by the early Keck observation (Knust et al. 2017). This SED yields $\beta = 0.50 \pm 0.09$, in good agreement with our late-time SED. This likely indicates some intrinsic afterglow variability during the early plateau phase which is not captured by our broken power-law fit.

B3 GRB 160821B

Data have been taken from Lamb et al. (2019); Troja et al. (2019); Kasliwal et al. (2017); Jin et al. (2018) and the GCN Circulars (Breeveld & Siegel 2016). This short GRB at $z = 0.16$ (Lamb et al. 2019) is known for its secure detection of a kilonova (Lamb et al. 2019; Troja et al. 2019). It is also the only short GRB so far with an (albeit tentative) detection of VHE emission (Acciari et al. 2021). As much of the light curve is dominated by kilonova light, we use the X-ray observations of the afterglow (G. P. Lamb, priv. comm.) as a stand-in, similar to the analysis of Lamb et al. (2019). We convert the flux densities to pseudo-magnitudes and shift the earliest (post-extended emission) point to the contemporaneous early optical observations, which are unlikely to be influenced by kilonova emission ($t < 0.1$ days). We find that at later times ($t \approx 5 - 10$ days) the optical emission in the bluest available bands (g' and $F606W$) is in agreement with the shifted X-ray emission, indicating the kilonova emission has become very red and faded under the afterglow level in these bands. Spectral information is sparse, but a $r'i'z'$ SED from early-time data is fit well by a simple power-law with slope $\beta = 0.62 \pm 0.13$, therefore we assume no dust, in agreement with the localisation offset from its host galaxy.

B4 GRB 180418A

Data are taken from Becerra et al. (2019); Rouco Escorial et al. (2021) as well as GCN Circulars (Guidorzi et al. 2018; Choi et al. 2018; Horiuchi et al. 2018; Misra et al. 2018; Malesani et al. 2018; Schady 2018; Schady & Chen 2018; Troja et al. 2018). This is an

¹³ http://www.physics.unlv.edu/~liye/GRB/grb_cls.html

¹⁴ https://gcn.gsfc.nasa.gov/notices_s/682269/BA/

event with a very bright early afterglow (Becerra et al. 2019) whose classification is unclear, however, the arguments presented in Rouco Escorial et al. (2021) indicate it is likely a short GRB, therefore we include it in this sample. The redshift is also unknown, but the host galaxy underlying the afterglow is very faint, and Rouco Escorial et al. (2021) estimate $z \approx 1.0 - 1.5$; similar to GRB 150424A, we adopt $z = 1$ here. Using data starting 0.00417 days after the trigger (the early emission is dominated by what is likely a reverse-shock flash, Becerra et al. 2019), and host-subtracting the data from sources other than Rouco Escorial et al. (2021), we find that using a single-power law decay yields a decay slope of $\alpha = 0.926 \pm 0.003$, in general agreement with the decay slopes found in Becerra et al. (2019); Rouco Escorial et al. (2021). Scatter combined with small error bars leads to a statistically bad fit ($\chi^2/\text{d.o.f.} = 5.41$). We find this fit can be improved significantly ($\chi^2/\text{d.o.f.} = 3.32$) by a broken power-law with $\alpha_1 = 0.837 \pm 0.009$, $\alpha_2 = 1.121 \pm 0.014$, $t_b = 0.033 \pm 0.004$ days, $n = 10$ fixed, and no host. The $\Delta\alpha$ is likely too small, and the post-break decay too shallow, for this to be a jet break. The broad SED ($uvw2$, $uvm2$, $uvw1$, u , b , g' , v , r' , i' , z') shows some scatter, and is blue ($\beta = 0.43 \pm 0.17$) with no evidence for dust. The UVOT lenticular filters are somewhat depressed compared to the rest of the data, especially $uvw2$, which is what one would expect for $z \approx 1$.

B5 GRB 181123B

GRB 181123B was a high-redshift short GRB at $z = 1.754$ with a bright host galaxy and a faint afterglow detection (Paterson et al. 2020). It shows extended emission (Dichiara et al. 2021) and was rapidly observed in the radio bands (Rowlinson et al. 2021; Anderson et al. 2021). As there is only a single i' detection, we have no information on colour or potential line-of-sight extinction. However, as the redshift is nearly identical to that of GRB 160410A, we assume the same dRc to plot it in the $z = 1$ frame. Generally, the afterglow is significantly fainter and the host significantly brighter than in the case of GRB 160410A.

B6 Observed GRB Afterglows

Observationally, the afterglow of GRB 180418A, where the classification is unclear (but with more evidence pointing toward it being a Type I GRB) is the brightest at early times, followed by that of GRB 160410A. The afterglow of GRB 180418A lacks a plateau phase and at 0.1 days, the two afterglows are of the same magnitude; however, later on, GRB 180418A decays less rapidly. Several other afterglows of Type I GRBs, such as the late-rising GRB 060614 and the long-plateau GRB 150424A, are also brighter at late times.

APPENDIX C: PHOTOMETRIC DATA ON GRB 160410A

Our photometry for GRB 160410A is given in Tab. C1 as used for the light-curve and subsequent SED fitting.

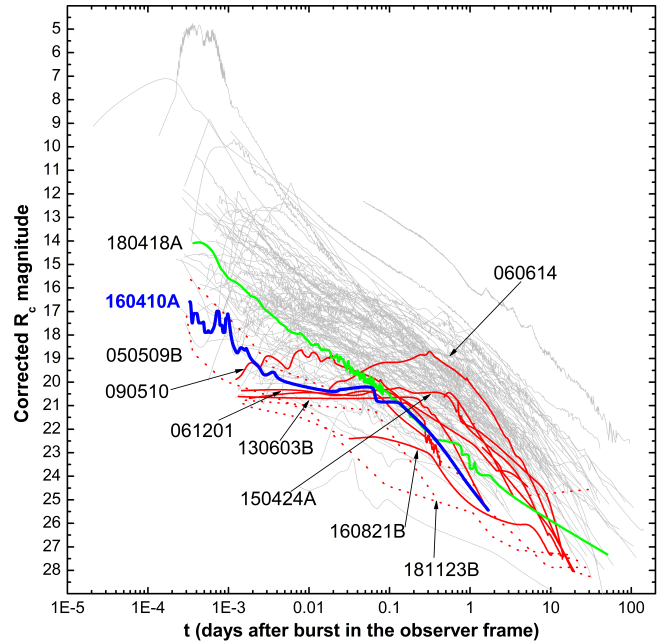


Figure B1. The afterglow of GRB 160410A (thick blue line) in the context of a large sample of GRB afterglows. Light curves are corrected for Galactic extinction but otherwise as observed. Thin grey lines are afterglows of Type II GRBs. Thicker red lines are a selection of afterglows of other Type I GRB. We have highlighted several. The optical afterglow of GRB 050509B was undetected, the “light curve” consists of deep upper limits only. GRB 060614 is a peculiar temporally long-lasting likely Type I GRB, the afterglow shows a very late peak. The other highlighted afterglows all show early plateau phases. The afterglow of GRB 160410A, seen to be one of the brightest ever detected (among afterglows of type I GRBs) at very early times, also evinces a plateau phase, but after an early steep decay.

Table C1: Photometry of the afterglow of GRB 160410A. Data are given in AB magnitudes and are not corrected for Galactic foreground extinction. Note that for UVOT data, the given exposure time is the total time coverage of each observation, for late-time data these values exceed the actual exposure time.

Time after burst (days)	Magnitude (AB)	Bin Width/ Exposure Time	Filter	Telescope/Instrument
0.062233	$21.884^{+0.670}_{-0.411}$	200	<i>uvw1</i>	<i>Swift</i> /UVOT
0.131352	$22.564^{+0.479}_{-0.331}$	900	<i>uvw1</i>	<i>Swift</i> /UVOT
0.641592	> 23.195	3001	<i>uvw1</i>	<i>Swift</i> /UVOT
0.003639	$20.349^{+1.399}_{-0.592}$	60	<i>u</i>	<i>Swift</i> /UVOT
0.003870	$19.848^{+0.713}_{-0.427}$	20	<i>u</i>	<i>Swift</i> /UVOT
0.004102	$20.280^{+1.200}_{-0.556}$	20	<i>u</i>	<i>Swift</i> /UVOT
0.004333	> 19.357	20	<i>u</i>	<i>Swift</i> /UVOT
0.064602	$21.289^{+0.468}_{-0.326}$	200	<i>u</i>	<i>Swift</i> /UVOT
0.140726	$21.893^{+0.394}_{-0.288}$	705	<i>u</i>	<i>Swift</i> /UVOT
0.532774	> 22.269	907	<i>u</i>	<i>Swift</i> /UVOT
0.716085	> 21.919	454	<i>u</i>	<i>Swift</i> /UVOT
0.050357	> 19.841	200	<i>b</i>	<i>Swift</i> /UVOT
0.066983	$20.842^{+0.680}_{-0.415}$	200	<i>b</i>	<i>Swift</i> /UVOT
0.540848	$22.142^{+2.779}_{-0.710}$	477	<i>b</i>	<i>Swift</i> /UVOT
0.023807	20.610 ± 0.057	198	g'_{GROND}	2.2m MPG/GROND
0.846850	24.440 ± 0.207	9715	g'_{GROND}	2.2m MPG/GROND
0.057488	> 19.510	200	<i>v</i>	<i>Swift</i> /UVOT
0.074104	$20.371^{+1.125}_{-0.541}$	200	<i>v</i>	<i>Swift</i> /UVOT
0.001169	$19.823^{+0.294}_{-0.231}$	20	<i>white</i>	<i>Swift</i> /UVOT
0.001400	$19.676^{+0.257}_{-0.207}$	20	<i>white</i>	<i>Swift</i> /UVOT
0.001632	$20.034^{+0.351}_{-0.265}$	20	<i>white</i>	<i>Swift</i> /UVOT
0.001864	$20.362^{+0.514}_{-0.348}$	20	<i>white</i>	<i>Swift</i> /UVOT
0.002095	> 20.081	20	<i>white</i>	<i>Swift</i> /UVOT
0.002440	$20.572^{+0.391}_{-0.287}$	40	<i>white</i>	<i>Swift</i> /UVOT
0.002731	$21.130^{+3.621}_{-0.733}$	10	<i>white</i>	<i>Swift</i> /UVOT
0.052726	$21.122^{+0.330}_{-0.253}$	200	<i>white</i>	<i>Swift</i> /UVOT
0.069352	$22.172^{+0.508}_{-0.345}$	200	<i>white</i>	<i>Swift</i> /UVOT
0.0003298	$16.8^{+0.5}_{-0.5}$	1	<i>r'</i>	0.25m TAROT
0.0003414	$16.8^{+0.5}_{-0.5}$	1	<i>r'</i>	0.25m TAROT
0.0003530	$18.0^{+0.5}_{-0.5}$	1	<i>r'</i>	0.25m TAROT
0.0003645	$17.3^{+0.7}_{-0.5}$	1	<i>r'</i>	0.25m TAROT
0.0003761	$17.3^{+0.7}_{-0.5}$	1	<i>r'</i>	0.25m TAROT
0.0003877	$17.3^{+0.7}_{-0.5}$	1	<i>r'</i>	0.25m TAROT
0.0003993	$17.3^{+0.7}_{-0.5}$	1	<i>r'</i>	0.25m TAROT
0.0004108	$17.3^{+0.7}_{-0.5}$	1	<i>r'</i>	0.25m TAROT
0.0004224	$17.7^{+0.7}_{-0.5}$	1	<i>r'</i>	0.25m TAROT
0.0004340	$17.7^{+0.7}_{-0.4}$	1	<i>r'</i>	0.25m TAROT
0.0004456	$17.7^{+0.7}_{-0.4}$	1	<i>r'</i>	0.25m TAROT
0.0004571	$17.7^{+0.7}_{-0.4}$	1	<i>r'</i>	0.25m TAROT
0.0004687	$17.7^{+0.7}_{-0.4}$	1	<i>r'</i>	0.25m TAROT
0.0004803	$17.7^{+0.7}_{-0.4}$	1	<i>r'</i>	0.25m TAROT

Table C1: continued.

Time after burst (days)	Magnitude (AB)	Bin Width/ Exposure Time	Filter	Telescope/Instrument
0.0004919	17.6 ^{+0.7} _{-0.4}	1	<i>r'</i>	0.25m TAROT
0.0005034	18.1 ^{+0.2} _{-0.6}	1	<i>r'</i>	0.25m TAROT
0.0005150	18.1 ^{+0.2} _{-0.6}	1	<i>r'</i>	0.25m TAROT
0.0005266	18.1 ^{+0.2} _{-0.6}	1	<i>r'</i>	0.25m TAROT
0.0005382	18.1 ^{+0.2} _{-0.6}	1	<i>r'</i>	0.25m TAROT
0.0005497	18.1 ^{+0.2} _{-0.6}	1	<i>r'</i>	0.25m TAROT
0.0005613	18.0 ^{+0.2} _{-0.6}	1	<i>r'</i>	0.25m TAROT
0.0005729	18.1 ^{+0.1} _{-0.7}	1	<i>r'</i>	0.25m TAROT
0.0005845	18.1 ^{+0.1} _{-0.7}	1	<i>r'</i>	0.25m TAROT
0.0005960	18.1 ^{+0.1} _{-0.7}	1	<i>r'</i>	0.25m TAROT
0.0006076	18.1 ^{+0.1} _{-0.7}	1	<i>r'</i>	0.25m TAROT
0.0006192	18.1 ^{+0.1} _{-0.7}	1	<i>r'</i>	0.25m TAROT
0.0006308	18.0 ^{+0.1} _{-0.7}	1	<i>r'</i>	0.25m TAROT
0.0006423	> 18.1	1	<i>r'</i>	0.25m TAROT
0.0006539	> 18.1	1	<i>r'</i>	0.25m TAROT
0.0006655	> 18.1	1	<i>r'</i>	0.25m TAROT
0.0006771	> 18.1	1	<i>r'</i>	0.25m TAROT
0.0006886	> 18.1	1	<i>r'</i>	0.25m TAROT
0.0007002	> 18.1	1	<i>r'</i>	0.25m TAROT
0.0007118	17.2 ^{+0.5} _{-0.4}	1	<i>r'</i>	0.25m TAROT
0.0007234	17.2 ^{+0.5} _{-0.4}	1	<i>r'</i>	0.25m TAROT
0.0007349	17.2 ^{+0.5} _{-0.4}	1	<i>r'</i>	0.25m TAROT
0.0007465	17.2 ^{+0.5} _{-0.4}	1	<i>r'</i>	0.25m TAROT
0.0007581	17.2 ^{+0.5} _{-0.4}	1	<i>r'</i>	0.25m TAROT
0.0007697	17.4 ^{+0.6} _{-0.3}	1	<i>r'</i>	0.25m TAROT
0.0007812	17.8 ^{+0.6} _{-0.5}	1	<i>r'</i>	0.25m TAROT
0.0007928	17.8 ^{+0.6} _{-0.5}	1	<i>r'</i>	0.25m TAROT
0.0008044	17.8 ^{+0.6} _{-0.5}	1	<i>r'</i>	0.25m TAROT
0.0008160	17.8 ^{+0.6} _{-0.5}	1	<i>r'</i>	0.25m TAROT
0.0008275	17.8 ^{+0.6} _{-0.5}	1	<i>r'</i>	0.25m TAROT
0.0008391	17.8 ^{+0.6} _{-0.5}	1	<i>r'</i>	0.25m TAROT
0.0008507	18.1 ^{+0.3} _{-0.6}	1	<i>r'</i>	0.25m TAROT
0.0008622	18.1 ^{+0.3} _{-0.6}	1	<i>r'</i>	0.25m TAROT
0.0008738	18.1 ^{+0.3} _{-0.6}	1	<i>r'</i>	0.25m TAROT
0.0008854	18.1 ^{+0.3} _{-0.6}	1	<i>r'</i>	0.25m TAROT
0.0008970	18.1 ^{+0.3} _{-0.6}	1	<i>r'</i>	0.25m TAROT
0.0009085	18.1 ^{+0.3} _{-0.6}	1	<i>r'</i>	0.25m TAROT
0.0009201	17.5 ^{+0.7} _{-0.4}	1	<i>r'</i>	0.25m TAROT
0.0009317	17.5 ^{+0.7} _{-0.4}	1	<i>r'</i>	0.25m TAROT
0.0009433	17.5 ^{+0.7} _{-0.4}	1	<i>r'</i>	0.25m TAROT
0.0009548	17.5 ^{+0.7} _{-0.4}	1	<i>r'</i>	0.25m TAROT
0.0009664	17.5 ^{+0.7} _{-0.4}	1	<i>r'</i>	0.25m TAROT
0.0009780	17.1 ^{+0.6} _{-0.4}	1	<i>r'</i>	0.25m TAROT

Table C1: continued.

Time after burst (days)	Magnitude (AB)	Bin Width/ Exposure Time	Filter	Telescope/Instrument
0.0009896	> 17.9	1	r'	0.25m TAROT
0.0010011	> 17.9	1	r'	0.25m TAROT
0.0010127	> 17.9	1	r'	0.25m TAROT
0.005347	20.249 ± 0.037	5	r'	8.2m VLT/X-shooter
0.713489	23.944 ± 0.042	2700	r'	2.5m NOT/ALFOSC
1.677059	25.649 ± 0.291	3600	r'	2.5m NOT/ALFOSC
44.683899	> 27.450	1800	r'	10.4m GTC/OSIRIS
0.023807	20.533 ± 0.065	198	r'_{GROND}	2.2m MPG/GROND
0.849788	24.573 ± 0.312	10440	r'_{GROND}	2.2m MPG/GROND
0.023807	20.726 ± 0.089	198	i'_{GROND}	2.2m MPG/GROND
0.849788	23.702 ± 0.294	10875	i'_{GROND}	2.2m MPG/GROND
0.023807	20.194 ± 0.108	198	z'_{GROND}	2.2m MPG/GROND
0.853656	> 23.395	10440	z'_{GROND}	2.2m MPG/GROND
0.023906	> 20.383	180	J'_{GROND}	2.2m MPG/GROND
0.849844	> 21.510	9600	J'_{GROND}	2.2m MPG/GROND
0.023906	> 19.905	180	H'_{GROND}	2.2m MPG/GROND
0.865926	> 20.976	9720	H'_{GROND}	2.2m MPG/GROND
0.023906	> 19.116	180	K'_{GROND}	2.2m MPG/GROND
0.849844	> 19.066	9360	K'_{GROND}	2.2m MPG/GROND
499.651238	> 24.740	3600	$3.6 \mu\text{m}$	<i>Spitzer</i> /IRAC

APPENDIX D: SED FIT FOR THE GRB 201221D HOST

This paper has been typeset from a \LaTeX file prepared by the author.

Best model for GRB201221D
($z=1.04$, reduced $\chi^2=0.45$)

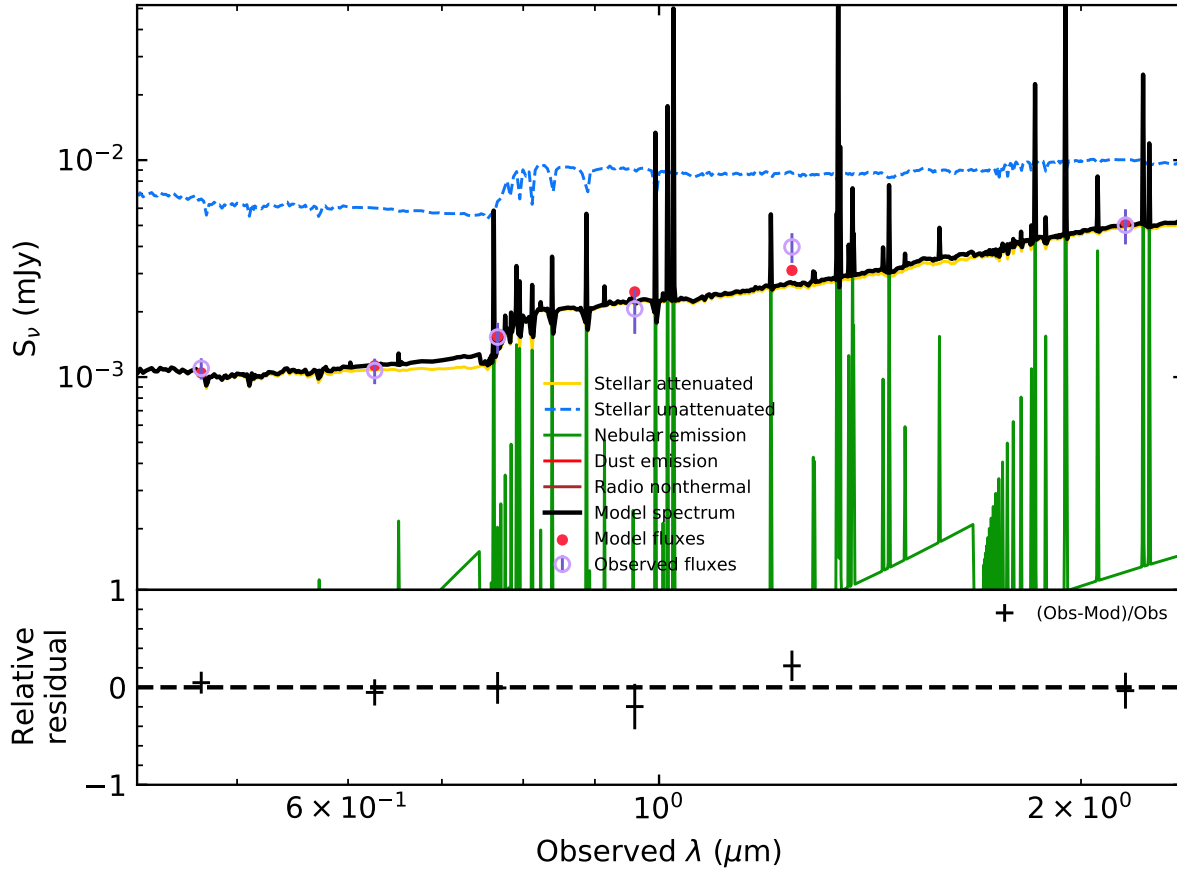


Figure D1. Best-fit SED modelling of the host of GRB 201221D. The upper panel shows the flux density distribution for the performed SED fitting with the photometry presented in Tab.3 and the lower panel the corresponding residuals.